Available online at www.sciencedirect.com

ScienceDirect

Proceedings of the Combustion Institute 38 (2021) 83–119

Proceedings of the Combustion Institute

www.elsevier.com/locate/proci

Understanding cool flames and warm flames

Yiguang Ju

Department of Mechanical and Aerospace Engineering, Princeton University, Princeton, NJ 08544, USA

Received 7 November 2019; accepted 20 September 2020
Available online 21 October 2020

Abstract

Low-temperature flames such as cool flames, warm flames, double flames, and auto-ignition assisted flames play a critical role in the performance of advanced engines and fuel design. In this paper, an overview of the recent progresses in understanding low-temperature flames and dynamics as well as their impacts on combustion, advanced engines, and fuel development will be presented. Specifically, at first, a brief review of the history of cool flames is made. Then, the recent experimental studies and computational modeling of the flame structures, dynamics, and burning limits of non-premixed and premixed cool flames, warm flames, and double flames are presented. The flammability limit diagram and the temperature-dependent chain-branching reaction pathways, respectively, for hot, warm, and cool flames at elevated temperature and pressure will be discussed and analyzed. After that, the effect of low temperature auto-ignition of auto-igniting mixtures at high ignition Damköhler numbers at engine conditions on the propagation of cool flames, warm flames, and double flames as well as turbulent flames will be discussed. Finally, a new platform using low temperature flames for the development and validation of chemical kinetic models of alternative fuels will be presented. Discussions of future research of the dynamics and control of low temperature flames under engine conditions will be made.

Keywords: Cool flames; Warm flames; Double flames; Low temperature combustion; Auto-ignition assisted flames

1. Introduction

The recent IPCC climate change report [1] calls for urgent action to cut CO_2 emissions by 45% by 2030 from the 2010 level and to limit the global temperature rise to 1.5 °C. One of the viable solutions to reduce CO_2 is to drastically improve engine efficiency and to use low carbon fuels [2–6]. In order to improve gasoline and diesel engine efficiency from today's approximately 38% to 60% for carbon reduction and to compete with electric vehicles [3,7], it is critical to establish lean burn and low temperature combustion technologies. As such, cool flames and warm flames, which have lower peak flame temperature and different chemistry pathways compared to hot flames have received renewed interest in research because of its strong relevance to engine knock, ignition and emission control, lean burn, flame stabilization, and low carbon fuel development [2–5,8–16].

Phenomenologically, a cool flame is a faint blue luminescent reaction front which partially oxidizes fuel into aldehydes, alkenes, and other intermediate

E-mail address: yju@princeton.edu

https://doi.org/10.1016/j.proci.2020.09.019

Nomenclature

ACI	advanced compression ignition
ASOI	after the start of injection
CARAT	co-flow axisymmetric reactor assisted turbulent burner
CFE	cool flame extinction limit
Da	Damköhler number
DME	dimethyl ether
EGR	exhaust gas recirculation
FLEX	flame extinguishment experiment
HCCI	homogenous charge compression ignition
HFE	hot flame extinction limit
HTC	high temperature chemistry
HTI	high temperature ignition
IPCC	intergovernmental panel on climate change
ITC	intermediate temperature chemistry
ITI	intermediate temperature ignition
LTC	low temperature chemistry
LTI	low temperature ignition
MON	motor octane number
NTC	negative temperature coefficient
PPCI	partially premixed compression ignition
PRF	primary reference fuels
PLIF	planar laser induced fluorescence
RATS	reactor-assisted turbulent slot burner
RCCI	reactivity controlled compression ignition
RON	octane number
SACI	spark-assisted compression ignition
SI	spark ignition
S_L	laminar flame speed
SIP	science innovation project
UHC	unburned hydrocarbons
δ	flame thickness
	equivalence ratio
τ	flow residence time or ignition delay time

small hydrocarbons with a small temperature rise (200–300 K) and low flame temperature (typically below 800 K) [17–27]. A warm flame has two luminescent reaction fronts, a faint blue cool flame front and a slightly brighter blue reaction front which further converts some of the partially oxidized intermediate products from the cool flame such as aldehydes into CO and H_2O with a moderate flame temperature (typically between 800-1100 K). A hot flame is a strong luminescent reaction front which converts fuel and/or partially oxidized fuel fragments into CO_2 and H_2O at a high flame temperature (typically 1100-2500 K) with strong combustion exothermicity. Under high pressure

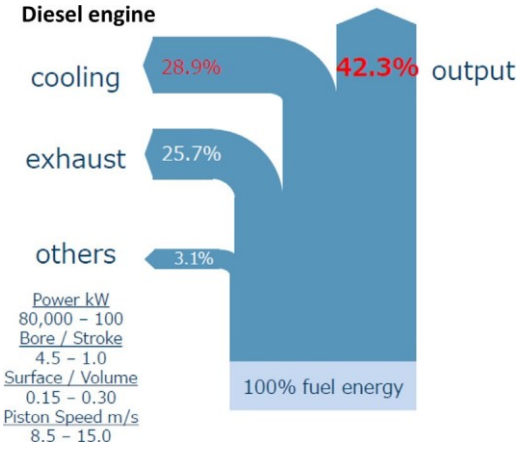

Fig. 1. Schematic of heat balance of an automotive diesel engine (Courtesy by Shuji Kimura, 2017).

and elevated temperature, cool flame and warm flame often occur earlier than the hot flame. Therefore, the dynamics of cool flame and warm flame will dramatically affect the burning limits and properties of hot flames and engine performance.

1.1. Advanced engines and low temperature combustion

Most of the commercial vehicles on the road today has net thermal efficiency below 40% [2,3]. Figure 1 shows a schematic of the energy input, output, and losses of an advanced diesel engine [3]. It is seen that with 100% of fuel energy input, the net output thermal efficiency is only 42.3%. The energy loss in cooling alone accounts for 28.9%. If one assumes the engine peak flame temperature is about 2400 K and the engine compression ratio is 16, the Carnot and Otto cycle efficiencies of this engine will be, respectively, 87% and 70%. Therefore, the engine thermal efficiency is limited neither by the Carnot cycle efficiency nor the Otto cycle efficiency, rather by the heat losses from the high temperature flames to engine walls and the exhaust gas. As such, in order to improve engine efficiency and drastically reduce the thermal losses, various low temperature combustion technologies such as the advanced lean burn gasoline engines [2,3,28], advanced compression ignition (ACI) and spark-assisted compression ignition (SACI) [29,30], homogenous charge compression ignition (HCCI) engines [4,5,31], reactivity controlled compression ignition (RCCI) engines [5], and partially premixed compression ignition (PPCI) engines [14,32,33] have attracted great attention. To realize these new technologies, it is important to understand the chemistry and dynamics of low temperature combustion.

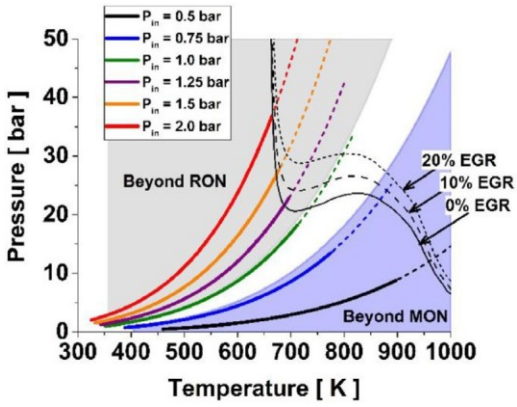

Fig. 2. Schematic of the gasoline engine pressure and temperature histories of a typical modern SI engine with 0–20% exhaust gas recirculation (EGR) overlaid with 8 ms ignition delay time of the alkylate fuel [28].

Fig. 3. Achieved engine net thermal efficiency of lean burn gasoline engine by the SIP program in Japan [2].

Figure 2 shows a schematic of the pressure and temperature histories of a typical modern spark ignition (SI) engine with different levels (0–20%) of exhaust gas recirculation (EGR) overlaid with 8 ms ignition delay time of the alkylate fuel [28] (an estimated timescale of ignition in engine). It is clearly seen that the engine operation between the octane number (RON) and the Motor Octane Number (MON) falls right to the region of cool flame, negative temperature coefficient (NTC), and warm flame regimes in a broad range of engine inlet pressure. The results showed that under these conditions, increasing EGR significantly changes the ignition delay time and the attenuation of knock. As such, understanding of cool flame and warm flame dynamics is critical to develop efficient engines and alternative fuels by suppressing engine knock and achieving reliable ultra-lean combustion.

Figure 3 shows the recent progress of the lean-burn gasoline engine efficiencies achieved by the engine science innovation project (SIP) of Japan [2]. It is seen that by using the super lean burn technology with engine knock and combustion control, the net engine thermal efficiency was increased from 38.5% to 51.5% between 2014 and 2018, highlighting the significant impact of low temperature combustion technology on engine efficiency.

In the studies of diesel engines, Musculus et al. [14] showed a conceptual model of different combustion modes for single-injection, PPCI low-temperature heavy-duty direct injection diesel combustion (Fig. 4). It is seen from Fig. 4 that in the early stage of fuel injection and before the high temperature ignition, the first stage low temperature ignition effectively oxidized the fuel into intermediate species such as CH_2O, H_2O_2, CO, and other unburned hydrocarbons (UHCs). This conceptual model of direct injection diesel combustion also clearly illustrates that cool flame chemistry plays a critical role in the combustion processes of PPCI engines.

A more clear experimental evidence of the cool flame formation of diesel fuel injection into a high temperature compressed air is the time-dependent schlieren and CH_2O PLIF imaging of *n*-dodecane spray injected into high-temperature air at 60 atm by Skeen et al. [34]. In Fig. 5, it is seen from the CH_2O time sequence that a cool flame appeared at the upper and lower lobes of the spray boundary at 190 μs after the start of injection (ASOI). At 240 μs ASOI, the cool flame front indicated by CH_2O image propagated into the core of the spray jet. This experiments clearly showed that a cool flame was initiated in a fuel lean high temperature region following the strong temperature dependence of the Arrhenius reaction rate equation and then propagated into the fuel rich mixtures. As such, it would be necessary to understand: 1) How fast does a cool flame propagate? 2) How different are the burning limits of cool flames from hot flames? 3) How will the flame stretch and molecular and turbulent transport processes affect the cool flame propagation speed? 4) When does a cool flame transfer to a warm flame or a hot flame? And 5) how can one establish a stable cool flame or warm flame in laboratory to examine its dynamics and chemistry?

Also, in the development of alternative jet fuels for gas turbine engines, Colket and co-workers studied the correlation between the derived cetane number and the lean blow-off limit for different kinds of fuels [10,16,35]. It is seen that the lean blow-off limit depends approximately linearly on the cetane number. Note that the cetane number is an indicator of low temperature fuel reactively while the blow-off limit is a property of flame speed or extinction limit. The approximate linear correlation in Fig. 6 suggests that the cool flame chemistry may also play a role in extending the flame stabilization limit via either cool flames or auto-ignition assisted flames. Then, the question becomes: how

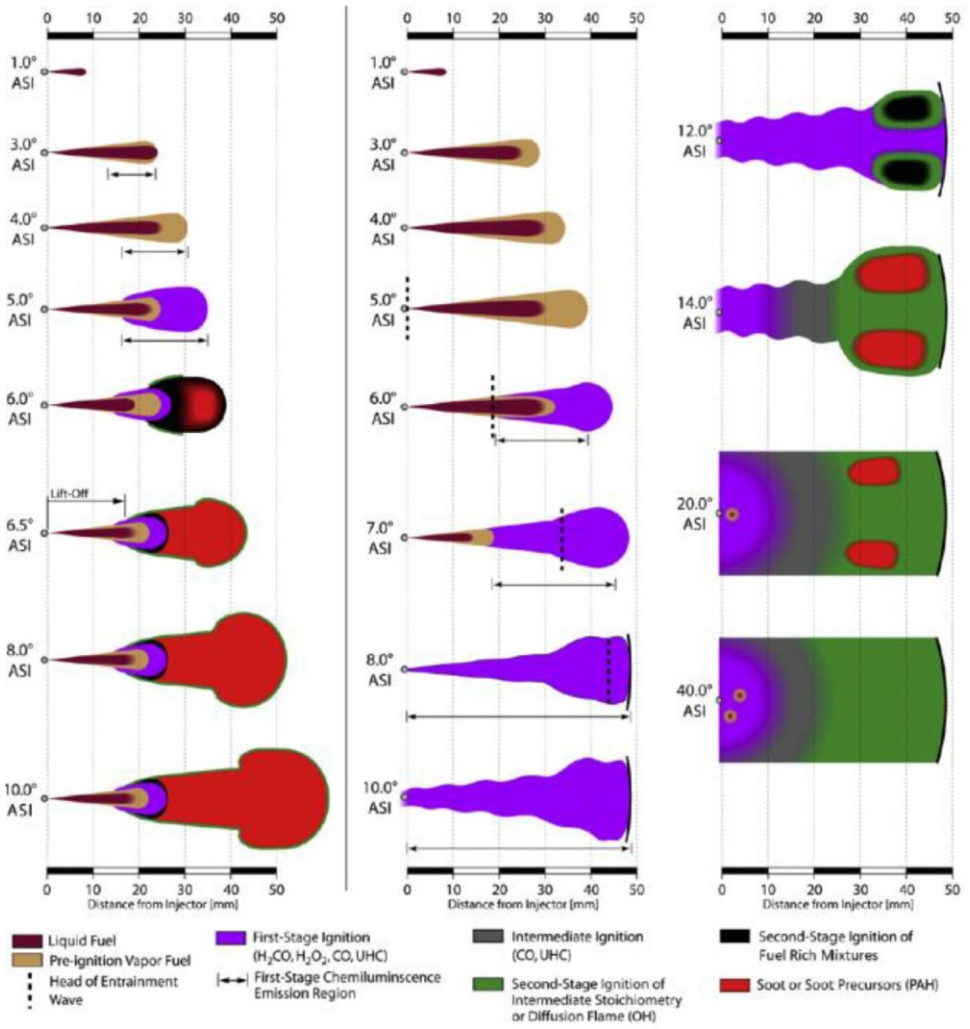

Fig. 4. Conceptual model for single-injection, PPCI low-temperature heavy-duty direct injection diesel combustion [14].

does the cool flame propagation speed depend on auto-ignition in an auto-igniting mixture?

1.2. History of cool flame studies and categorization of different flame regimes

Mastering fire is the history of civilization of mankind. The milestone of the cool flame and warm flame studies is schematically shown in Fig. 7. In million years ago, mankind discovered the use of fire, which was a hot flame. Fire was used in making food and tools, and killing bacteria. About 200 years ago, Davy [17] and Perkin [18,36] discovered that a very faintly luminous bluish cool flame played round a heated metal surface when a rich ether and hexane-air mixture was impinged on. In the cool flame, significant amount of aldehydes were observed but little CO_2 was formed [22,23,37–43].

Interested in the cool flame phenomena, extensive studies of cool flames have been conducted from 1920s to 1980s. Many of these studies were focused on the cool flame flammability limits and oscillations as a function of fuels, temperature, and pressure at fuel rich conditions [19,22–26,37–46]. In 1940s, a two-stage blue flame was also observed, respectively, in preheated tubes and on flat burners [22–26,38,47]. Figure 8 shows the spontaneous ignition limits and burning limits for cool flames and blue flames in comparison to hot flames of *n*-butane/oxygen/nitrogen mixtures by Williams et al. [24–26] in a preheated vertical tube with precise temperature control and over a wide range of compositions. It is seen that the cool flame spontaneous ignition limit was far exceeded that of the hot flame

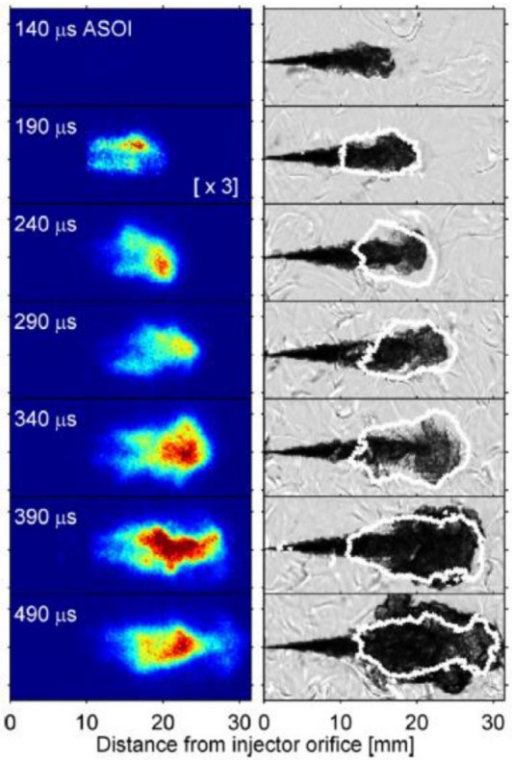

Fig. 5. Time histories of CH_2O PLIF images (left) and schlieren images (right) for *n*-dodecane spray injection into high-temperature air at 60 atm [34].

on the fuel rich side. However, on the fuel lean side, the ignition limit of the cool flame was narrower than that of the hot flame. Detailed reviews of cool flame studies of premixed rich fuel mixtures before 1980s can be found in [20,21,46].

In 1990s, microgravity combustion for space applications attracted great attention and many

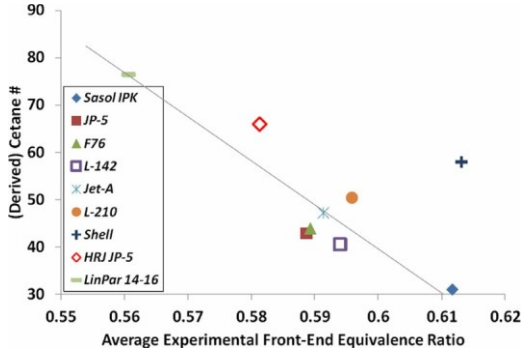

Fig. 6. Measured correlation between the derived cetane number and the lean blow-off limits of different jet fuels [35].

gaseous flames and droplet combustion experiments were carried by using drop towers, parabolic flights, space station, and space shuttles [48–54]. In 1999, a pioneering microgravity experiment of premixed cool flames was conducted by Foster and Pearlman [55–58] aboard NASA's KC-135 aircraft. The experiments successfully captured the unsteady outwardly propagating spherical cool flames of fuel rich propane and butane mixtures after auto-ignition at elevated temperatures.

Recently, due to the shift of research interest on fuel efficiency and carbon emissions, the focus of cool flame studies was changed to low temperature non-premixed combustion and fuel lean premixed combustion. With the development of low temperature kinetic models [59–61], numerical simulations of non-premixed cool flames started in 1990s. In 1995, Tanabe et al. [62] conducted numerical simulations of n-heptane droplet combustion in an oxygen-helium environment. The results showed that there was a two-stage temperature rise due to cool flame and high temperature ignition,

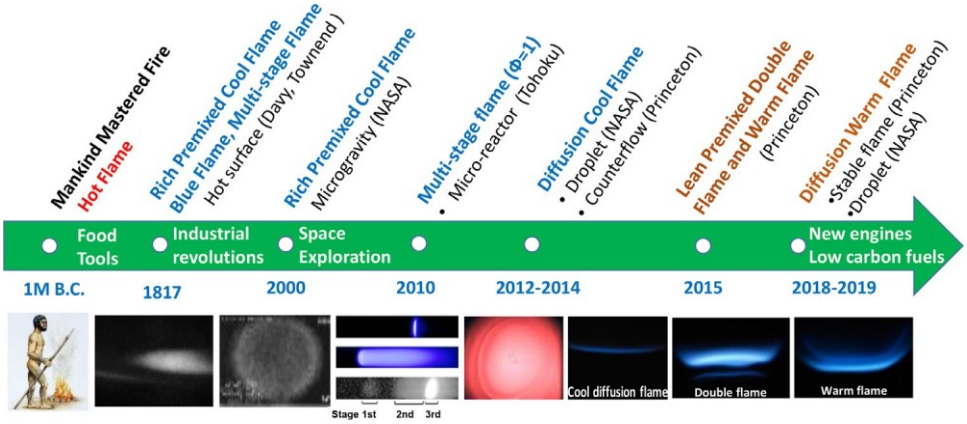

Fig. 7. Schematic of the history for observing cool flames, warm flames, double flames, and multi-staged flames.

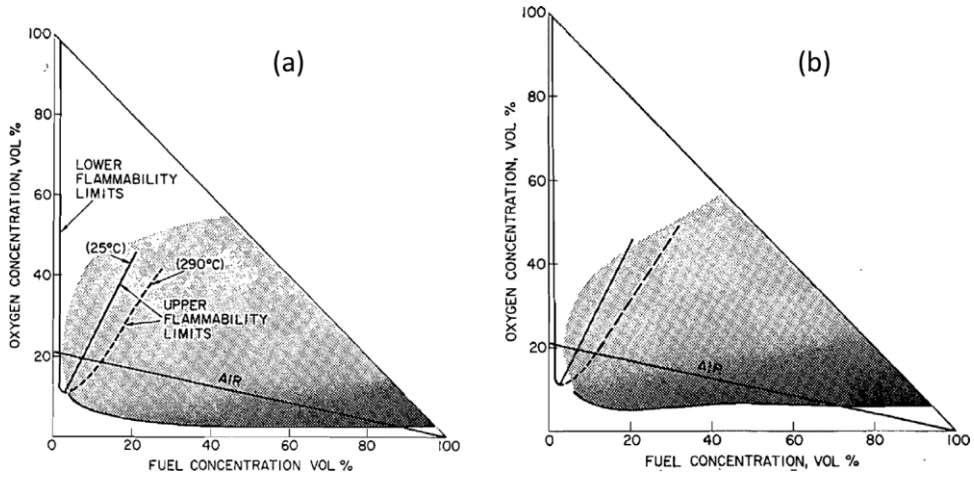

Fig. 8. (a) Spontaneous ignition limits of *n*-butane cool flames (shaded area) and (b) blue flame composition limit with nitrogen dilution at 1 atm and a temperature of 663 ±20 K. The lines indicate the lower and upper flammability limits of hot flames.

respectively. In 2005, Cuoci et al. [63] conducted similar simulations of *n*-heptane droplet ignition. The results showed that a cool flame is formed after the radiative extinction of a hot flame. In 2011, Ju et al. computationally modelled an ultra-lean n-heptane/air mixture under spark assisted HCCI conditions [29]. The results demonstrated that a spark assisted hot flame can transfer into a double flame structure with a leading cool flame and a trailing hot flame. In 2012, Law and Zhao [64] computationally modeled low temperature combustion in a diffusive n-heptane/air counterflow geometry. The results showed that there was an NTC effect which resulted in multiple flame branches and that an increase of pressure extended the low temperature flame branch to lower temperature. Nevertheless, experimental observation of cool flames in a non-premixed system or fuel lean mixture were not reported before 2010.

Since 2010, breakthroughs in laminar cool flame and warm flame experiments in non-premixed combustion and for fuel lean mixtures have been achieved by using heated micro-flow reactors [65–69], microgravity droplet experiments [70–81], counterflow flames [27,82–96], and flat flame burners [97]. For example, as shown in Fig. 7, in 2010, in the study of microscale combustion, Oshibe et al. [65] observed a three-stage flame structure in a preheated micro-channel for a stoichiometric dimethyl ether/air mixture. In 2012, in droplet Flame Extinguishment Experiments (FLEXs) on board the International Space Station, Nayagam and the NASA microgravity team observed that a diffusion cool flame might be formed after the radiation extinction of the hot flame with a large n-heptane droplet. In 2013, in plasma assisted combustion, Ju and co-workers succeeded in the establishment of self-sustaining diffusion cool flames by plasma and ozone sensitization [82,83,96] in a counterflow. At the same time, Law and co-workers observed the NTC affected weakly burning diffusion flame in counterflow with heated air [92]. In 2015, Reuter et al. [84,85,98] observed premixed cool flames in sub-limit fuel lean mixtures. Moreover, a premixed double flame structure with a leading cool flame and a trailing hot flame similar to the prediction in [29] was also observed experimentally at conditions slightly above the fuel lean burn limit of the hot flame [84,98]. In a more recent shock tube experiment, spherically expanding transient iso-octane double flames were observed by Hanson and co-workers [99] at near stoichiometric conditions. In addition, twin cool flames in a partially premixed counterflow were also observed [85]. Furthermore, in 2018, Yehia et al. [100,101] experimentally observed a warm diffusion flame structure in both ether and alkane counterflow diffusion flames. At the same time, an independent NASA microgravity experiment also revealed the existence of a warm flame in droplet combustion. In a more recent experiment study, Zhou et al. [102] further revealed that NO_x addition in the oxidizer stream also promoted the formation of n-dodecane diffusion warm flame. More recently, non-premixed turbulent jet cool flames were also successfully established experimentally [103,104].

The success in experimental observation of cool flames and warm flames further ignites the enthusiasm of numerical modeling of low temperature flames. Numerical modeling and theoretical analysis of laminar diffusion cool flames, warm flames, and double flames were conducted, respectively, in spherically propagating flame [29,105–108], planar propagating flames [91,109,110], counterflow flames [64,83,90,111–114], droplet combustion [62,70–72,74,76–79,115–119], lifted laminar

Table 1
Characterization of different premixed and non-premixed flame regimes using mixture equivalence ratio, flame chemistry, flame temperature, and the number of flame zones. $_{0,l}$: Lean burn limit of hot flames, $_{0,r}$: Rich burn limit of hot flames. LTI: low temperature ignition, ITI: intermediate temperature ignition, HTI: high temperature ignition.

Different flame regimes in low and high temperature combustions						
Flame regimes		Mixture	Equiv. Ratio	Chemistry	Temp., K	Flame zones
Cool Flame		**Premixed**	$> {}_{0,r}$ $_{0,l} < < {}_{0,r}$ $< {}_{0,l}$	LTC	500–800	1
		Diffusion/Non-premixed	LTC	500–800	1 or 2	
Warm Flame	Blue flame	**Premixed**	$_{0,r} \geq$	LTC, ITC	800–1100	2–3
	Warm flame	**Premixed**	$< {}_{0,l}$	LTC, ITC	800–1100	2
		Diffusion		LTC, ITC	800–1100	2
Hot Flame		**Premixed**	$_{0,l} < <$ $_{0,r}$ HTC		1100–2500	1
		Diffusion		HTC	1100–2500	1
Double flame*		**Premixed**	$_{0,l} < <$ $_{0,r}$ LTC, HTC		1100–1500	2
Three-stage flame*		**Premixed**	$_{0,l} < <$ $_{0,r}$ LTC, ITC, HTC		1100–1500	3

$_{0,l}$: Lean burn limit of hot flames, $_{0,r}$: Rich burn limit of hot flames.

flames and turbulent flames [94,103,120–124], and spray combustion [34,114,125]. These studies dramatically advanced the understanding of the dynamics and chemistry of cool flames, warm flames, and double flames.

The observed different flame regimes in premixed and non-premixed flame systems can be characterized by using the equivalence ratio, combustion chemistry, flame temperature, and the number of flame zones as shown in Table 1. It is seen that a premixed cool flame, which is governed by the low temperature chemistry (LTC), can be observed at an equivalence ratio either below, between, or above the lean and rich flammability limits of hot flames. However, the warm flame, which is governed by both LTC and intermediate temperature chemistry (ITC), only exists slightly above the fuel rich limit or below the lean limit of the hot flame, respectively. On the other hand, the double flame, which is governed by both LTC and high temperature chemistry (HTC), only exists between the lean and rich hot flame burning limits. The three-staged flame which is affected by all LTC, ITC, and HTC will also exist within the burning limits of a hot flame. Note that the temperature ranges of LTC, ITC, and HTC shown in Table 1 may vary with fuels, pressure, and even flow residence time.

Alternatively, the different flame regimes can also be characterized by using the ignition and flame Damköhler numbers (Da), respectively, as shown in Table 2. Here the subscripts of "ig" and "f" of Da, respectively, denote the ignition and flame; the subscripts of "L", "I", and "H" of Da_{ig} represent the ignition of LTC, ITC, and HTC, respectively; and the subscripts of "C" and "H" to Da_f denote, respectively, cool flame and hot flame. Also, τ_{res} and τ_{ig} are, respectively, the flow residence time and ignition delay time. S_L and δ denote, respectively, the laminar flame speed and flame thickness. It is well accepted that for ignition, LTI, ITI, and HTI occur, respectively, as their ignition Damköhler numbers approach or great than unity. Similarly, cool flame and hot flame also only exist when the flame Damköhler numbers are greater than unity and the corresponding ignition Damköhler numbers are far lower than unity. For warm flame, however, it exists when the cool flame Damköhler number is greater than unity and the ITI Damköhler number is also greater than unity. For auto-ignition assisted cool flame, the cool flame Damköhler number is great than unity and the ignition Damköhler number of LTI is also close to unity.

In practical engine combustion, the combustion mode can be either ignition, flame, or auto-ignition assisted combustion. As shown in Fig. 9, ignition is governed solely by combustion chemistry. The temperature dependent LTC, ITC, and HTC will govern the process of LTI, ITI, and HTI, respectively. On the other hand, flame is governed by both diffusion transport and ignition chemistry. Therefore, the coupling between diffusion transport and the temperature dependent combustion chemistry in flames will lead to different flame regimes such as cool flame, warm flame, hot flame, double flame, and the three-stage flame. In practical engines, the engine inlet pressure and temperature are very high which render the auto-ignition timescale comparable to the flow residence time. As such, the ignition Damköhler number becomes so large that auto-ignition in front of the flame may occur. In this case, the flame will become an auto-ignition assisted flame (Fig. 9 and Table 2). Particularly, when the mixture is chemically sensitized by plasma generated radicals, ozone, NO_x, and other active intermediate species in a recirculation zone or turbulent mixing, the ignition delay time is dramatically reduced so that the flame becomes mostly likely an auto-ignition assisted flame. Then, the

Table 2
Definition of the Damköhler numbers for LTI, ITI, HTI, cool flame, and hot flame as well as the corresponding Damköhler numbers of warm flame, double flame, and auto-ignition assisted cool flame.

Low Temp. Ignition (LTI)	Intermediate Temp. Ignition (ITI)	High Temp. Ignition (HTI)	Cool flame	Hot flame	Warm flame	Double flame	Ignition assisted cool flame
$Da_{ig,L} \geq 1$ $\tau_{res}/\tau_{ig,L}$	$Da_{ig,I} \geq 1$ $\tau_{res}/\tau_{ig,I}$	$Da_{ig,H} \geq 1$ $\tau_{res}/\tau_{ig,H}$	$Da_{f,C} > 1$ $\tau_{res} * S_{L,C}/\delta_{f,C}$	$Da_{f,H} > 1$ $\tau_{res} * S_{L,H}/\delta_{f,H}$	$Da_{f,C} > 1$ $Da_{ig,I} \sim 1$	$Da_{f,C} > 1$ $Da_{f,H} > 1$	$Da_{ig,C} > 1$ $Da_{f,C} > 1$

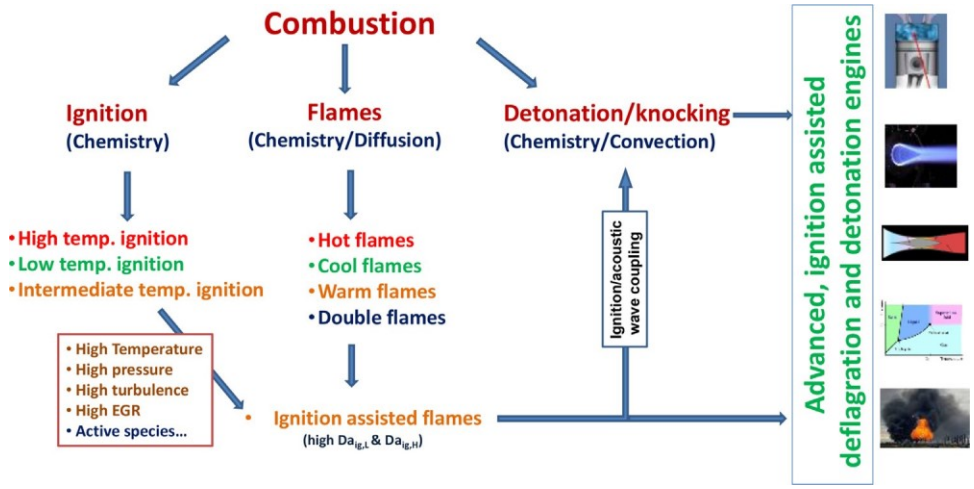

Fig. 9. Correlations between auto-ignition, flames, auto-ignition assisted flame, detonation, and engine combustion.

question is: how fast can an auto-ignition assisted cool flame propagate? In fact, as shown in Fig. 9, with the increase of auto-ignition Damköhler number, the speed of auto-ignition assisted flame increases rapidly and can result in strong combustion and acoustic wave coupling. When the heat release rate from the auto-ignition assisted flame becomes comparable or faster than the acoustic wave, it will generate a pre-flame shock wave and even lead to deflagration to detonation transition. Therefore, understanding different ignition and flame regimes and the auto-ignition assisted flame propagation involving cool flames and warm flames is critical to develop advanced engine concepts.

Several review papers have been published on cool flames [19–21,27]. Most of these reviews focused on early studies of cool flame ignition limits, unified kinetic models, and/or oscillatory cool flames in reactors. A recent review by Ju et al. [27] made a comprehensive overview of the recent studies of cool flame chemistry and dynamics. Since then, there are a number of interesting experiments and simulations have been conducted by different combustion research groups in the areas of auto-ignition assisted cool flames, outwardly propagating spherical double flames in a shock tube experiment, the minimum ignition energy as well as the stretch effect on cool flames, NO_x sensitized cool flame and warm flames, non-premixed turbulent cool flames, and analysis of cool flames. In this review, we will make a brief review of the dynamics and chemistry of cool flames and warm flames, and focus mainly on the recent understanding of auto-ignition assisted and chemically sensitized low temperature combustion. In the end of this review, the major challenges in understanding cool flames and warm flames will be discussed.

2. Temperature and composition dependent ignition and chain-branching pathways

Flame is an exothermic, luminescent, diffusion-ignition front with a chain-branching reaction process. To understand cool flames and warm flames, it is necessary to understand their temperature-dependent diffusion, ignition, and the major chain-branching pathways.

2.1. Temperature, pressure, and composition dependent ignition delay time

Auto-ignition delay time of large hydrocarbon or oxygenated fuels has been studied extensively by using shock tubes [126–129], rapid compression machines [130–133], and kinetic modeling

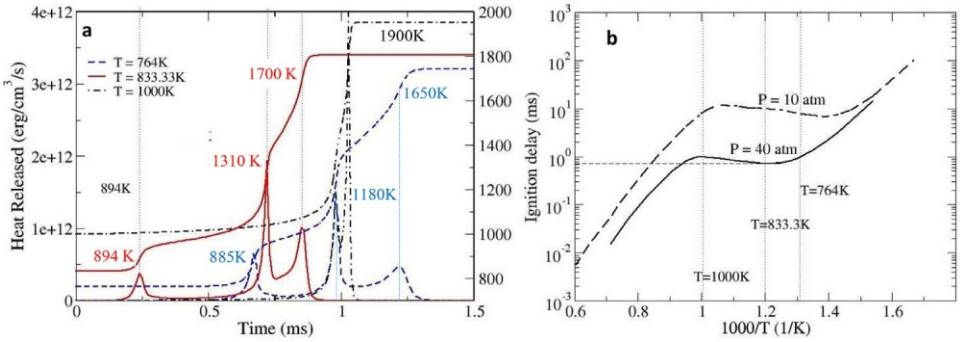

Fig. 10. a: Auto-ignition histories of temperature and the heat release rate of DME at ϕ0.3 and 40 atm at three different initial temperatures [144]. b: Dependence of ignition delay time on temperature at 10 and 40 atm [143]. The kinetic model was from [145].

[59,60,134–142]. Figure 10a shows the predicted time histories of temperatures and chemical heat release rates of dimethyl ether (DME)/air auto-ignition at equivalence ratio of ϕ0.3 and pressure of 40 atm [143,144] using the kinetic model of [145]. The initial temperatures are, respectively, 764, 833, and 1000 K. It is seen that for the initial temperature of 764 K, there are three heat release peaks, respectively, at 885, 1180, and 1650 K, indicating the occurrence of a three-stage auto-ignition process. These three distinctive heat release peaks correspond, respectively, to three temperature dependent chain-branching reactions of LTC, ITC, and HTC. When the initial temperature is raised to 833 K, the three heat release peaks still exist, respectively, at 894, 1310, and 1700 K, but the ignition delay time is shortened significantly. With a further increase of initial temperature to 1000 K, not only the ignition delay time is delayed but also the first LTC heat release peak disappears. In addition, the second stage ITC and the third stage HTC heat release peaks become very close. This increase of ignition delay time with temperature is the typical NTC effect. The disappearance of the LTI heat release peak is because the initial temperature is above the LTC. If the mixture temperature is further raised above the ITC temperature, only the third HTC heat release peak will exist. Therefore, the ignition of dimethyl ether involves LTC, ITC, and HTC and is strongly dependent of the initial temperature. Figure 10b plots the dependence of ignition delay time on the initial temperature at 10 and 40 atm, respectively. It is seen that there is a NTC region between the low temperature ignition branch and the high temperature ignition branch. In addition, an increase of pressure shifts the NTC region to a higher temperature.

To show the sensitivity of auto-ignition on chemical sensitization, Figure 11a shows the dependence of the ignition delay time on the initial temperature for a stoichiometric *n*-heptane/air mixture at 20 atm with and without 100 ppm OH addition. The solid and dashed lines, respectively, represent the ignition delay times of LTI and HTI. It is clearly seen that OH radical addition in the initial mixture can dramatically reduce the time of LTI to below100 μs. Thus, through chemical sensitization by active species such as OH, ozone, NO_x, plasma generated excited molecules, and EGR, LTI can be shortened dramatically, rendering the cool flame and warm flame to occur at a much shorter timescale. Figure 11b shows the dependence of predicted ignition delay time as a function of mixture fraction for non-premixed *n*-dodecane/air mixtures with air temperature of 960 K and fuel temperature of 450 K at pressure of 25 bar and oxygen concentration of 15% in the oxidizer stream [123]. It is seen that the delay time of LTI and HTI depends differently on the mixture fraction. The minimum ignition delay time of LTI occurs at a much lower mixture fraction than that of the HTI. This result suggests that in non-premixed combustion, an LTI may occur firstly at a lower mixture fraction, then resulting in a cool flame propagation into a fuel rich region until the HTI occurs [123].

2.2. Temperature-dependent chain-branching reaction pathways

As shown in Table 1, the flame regime can be categorized by using the governing chain-branching reaction pathways. Kinetic studies of the chain-branching process in cool flames started in 1940s. Barusch et al. [146] revealed that RO_2 and QOOH were responsible for cool flame chain-branching chemistry. Bailey and Norrish systematically studied the low-temperature oxidation kinetics of hexane in the cool flame region [39] and proposed a kinetic scheme for cool flames. In 1965, a skeletal low-temperature kinetic model was developed by Knox [147]. In 1988, Morley [148] used a laser perturbation method to understand the timescales of the mechanistic components of a cool flame. In 1990, Carlier et al. [149] conducted an experi-

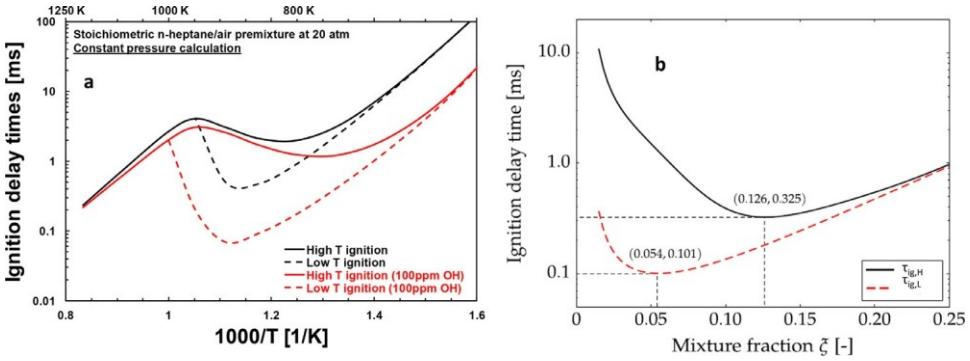

Fig. 11. (a) Dependence of the ignition delay time on the initial temperature for a stoichiometric *n*-heptane/air mixture at 20 atm with and without 100 ppm OH addition. (b) Ignition delay time as a function of mixture fraction for non-premixed *n*-dodecane/air mixtures with air temperature of 960 K and fuel temperature of 450 K at pressure of 25 bar and oxygen concentration of 15% in the oxidizer stream [123]. The kinetic model was from [29].

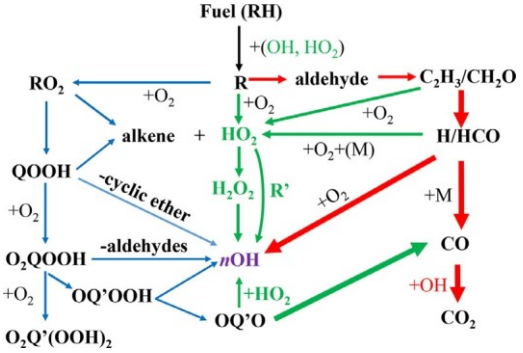

Fig. 12. A schematic of the key reaction pathways at different temperatures (blue arrow: Below 800 K; green arrow: 800-1100 K; red: above 1100 K).

mental study and computational modeling of the butane cool flame structures and the ignition in a rapid compression machine by using a semi-detailed chemical kinetic model. Detailed species information in cool flames was obtained. These early kinetic studies laid the foundation of the current understanding of LTC [60,141,150–152].

The schematic of temperature dependent chain-branching reaction pathways for fuel oxidation is shown in Fig. 12 [27,59,137,138,153]. At a low temperature (e.g. below 800 K), LTC chain-branching pathway governs the rate of fuel oxidation. As shown in Fig. 12, LTC fuel (RH) oxidation starts with an H-abstraction of fuel by a radical such as OH, O, HO_2 and forms a fuel radical (R). Then, the fuel radical (R) is added by an O_2 molecule to form RO_2. After that, the internal isomerization of RO_2 will lead to the formation of QOOH (hydroperoxyalkyl radical). The subsequent oxygen molecule addition to QOOH to form O_2QOOH and its beta scissions produce multiple OH radicals (Fig. 12). This LTC chain-branching pathway results in the

Table 3
HO_2 chemistry at intermediate temperature and high pressure for ITI and warm flame.

Fuel+HO_2=R + H_2O_2	**(R_1)**
Aldehyde+HO_2= H_2O_2+RCO	**(R_2)**
RO_2 ⟷ R + O_2	**(R_3)**
RO_2 → alkene + HO_2	**(R_4)**
QOOH→ cyclic ether + OH	**(R_{5a})**
→ alkene + HO_2	**(R_{5b})**
O_2QOOH→ QOOH+O_2	**(R_6)**
R + HO_2 = RO + OH	**(R_7)**
R + O_2 = aldehyde +HO_2	**(R_8)**
RCO+ O_2 = aldehyde + CO+OH	**(R_9)**
HO_2+CH_2O = H_2O_2+HCO	**(R_{10})**
HO_2+ HO_2 = H_2O_2+ O_2	**(R_{11})**
H_2O_2=2OH	**(R_{12})**

first stage low temperature ignition (Fig. 10a) and the cool flame. As such, the major cool flame chain-branching reaction pathway can be written as,

$$R \rightarrow RO_2 \rightarrow QOOH \rightarrow O_2QOOH \rightarrow OQ^{\prime}O + 2OH \quad (1)$$

Note that at longer flow residence time and higher pressure, it has been shown that more oxygen molecules can be added to O_2QOOH [154,155] to form a large oxygenated complex that can lead to additional chain-branching reactions.

At an intermediate temperature (e.g. 800-1100 K), as shown in Fig. 12 and Table 3, the decompositions of RO_2, QOOH, and O_2QOOH via $RO_2 \rightarrow R + O_2$ (R_3), QOOH → HO_2 + alkene or cyclic ether + OH (R_5), and O_2QOOH → QOOH + O_2 (R_6) shut down the O_2QOOH chain-branching pathway (Eq. (1)) and slow down the fuel reactivity, leading to the NTC effect in Fig. 10. As a result, in the NTC process, the concentrations of HO_2 and fuel radicals R will increase. Therefore, HO_2 reactions with fuel radicals (R_7) and partially oxidized intermediate species (R_2 and R_{10}) as

well as the H_2O_2 decomposition reaction (R_{12}) become the dominant pathway to produce OH radicals for chain-branching. As such, at an intermediate temperature, the HO_2 chemistry listed in Table 3 is the major chain-branching pathway for the second stage ITI shown in Fig. 10a and warm flame formation [74,100–102]. At high pressure, HO_2 chemistry plays an even greater role in fuel oxidation and shifts the NTC effect to higher temperature (Fig. 10) [156,157]. In summary, the major chain-branching reaction pathway for ITI and warm flame formation can be written as [27],

$$R^{\prime} + HO_2 \rightarrow R^{\prime}O + OH,\ CH_2O \rightarrow HCO \rightarrow HO_2 \rightarrow H_2O_2 \rightarrow 2OH \quad (2a)$$

$$R^{\prime}CO + O_2 \rightarrow \text{aldehyde} + CO + OH,\ CH_2O \rightarrow HCO \rightarrow HO_2 \rightarrow H_2O_2 \rightarrow 2OH \quad (2b)$$

At a higher temperature (above 1100 K), the radical production is governed by the key high temperature chain-branching reaction,

$$H + O_2 = OH + O \quad (3)$$

This branching reaction leads to the third stage HTI in Fig. 10a and the hot flame formation.

Therefore, since a flame is an exothermic, luminescent, diffusion-ignition front with chain-branching reactions, the three temperature dependent chain-branching reactions in Eqs. (1)–(3) determine that there will be three different flame regimes, the cool flame, warm flame, and hot flame.

3. Dynamics of cool flames and warm flames

Almost all cool flame studies before year 2000 had been focused exclusively on fuel rich premixed flames. Those studies can be found in several cool flame review papers [19–21,27]. In this paper, we only make a brief summary of the fuel rich cool flame studies before year 2000 and focus only on the recent studies for fuel lean premixed and non-premixed cool flames and warm flames.

3.1. Premixed cool flames, warm flames, and double flames

In 1940s, Townend and coworkers studied cool flame stabilization in a wall-heated quartz tube using rich aldehyde and ether/oxygen mixtures [38]. As shown in Fig. 13, at a lower pressure (300 mmHg), a single cool flame front was observed (Fig. 13a). When the pressure was increased to 400 mmHg, a second stage blue flame emerged behind the first stage cool flame. The second stage blue flame occurred due to the ITI. As such, following the categorization of the flame regimes in Tables 1-2, hereafter, the double luminescent flame

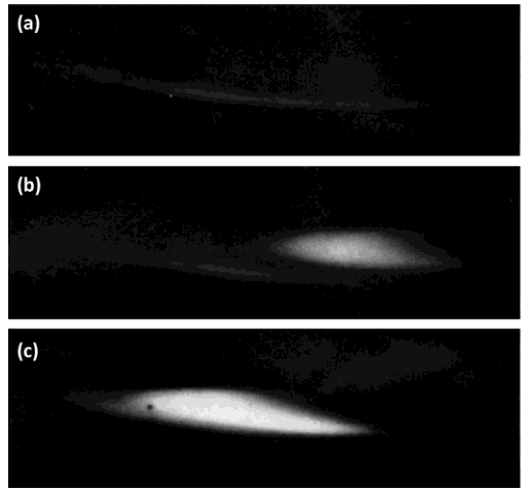

Fig. 13. Cool and blue flames stabilized in a heated quartz tube reactor of 80% CH_3CHO and 20% O_2 flowing from the left to the right at pressures of (a) cool flame at 300 mmHg, (b) cool flame and blue flame at 400 mmHg, and (c) merged flame at 600 mmHg [38].

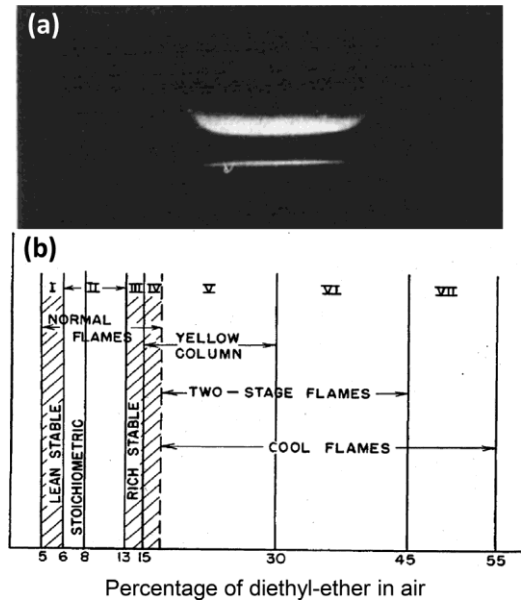

Fig. 14. (a) Image of the fuel rich diethyl ether/O_2/N_2/Ar (14.7/17.9/66.5/0.9) two-stage cool flame and blue flame at 1 atm [41]. (b) Flame regimes with the increase of percentage of fuel in air [47].

structure with a leading cool flame and a trailing ITI will be called as "warm flame". As the pressure was further increased to 600 mmHg, ITI via the HO_2 chemistry (Table 3) became faster and the first stage cool flame zone and the second stage blue flame zone started to merge, resulting in a more luminescence flame zone.

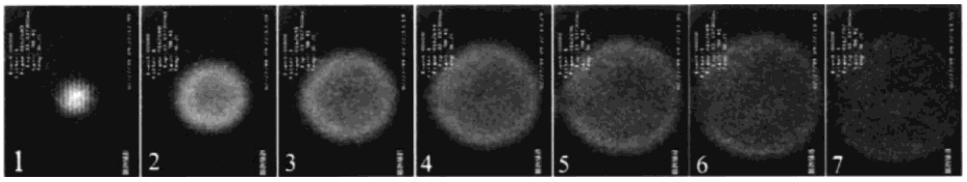

Fig. 15. Transient images of the flame development in microgravity with mixtures of 66.7% C_4H_{10}–33.3% O_2, $P_{initial}$=54.4 psia, T_{vessel} =310 °C with a time interval of 0.1 second [57].

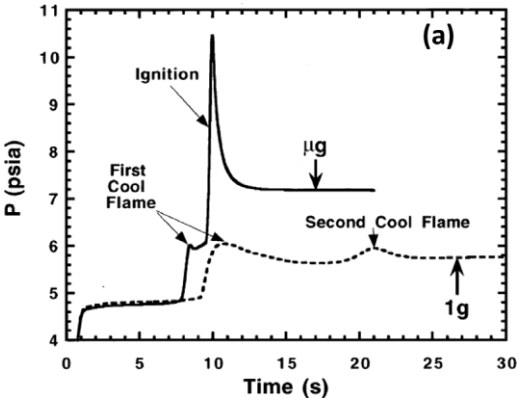

Fig. 16. (a) Comparison of pressure dependence of transient flame kernel development at normal gravity and microgravity for 66.7% C_4H_{10}–33.3% O_2 mixture at initial pressure of $P_{initial}$=4.4 psia and T_{vessel} = 310 °C [57,159].

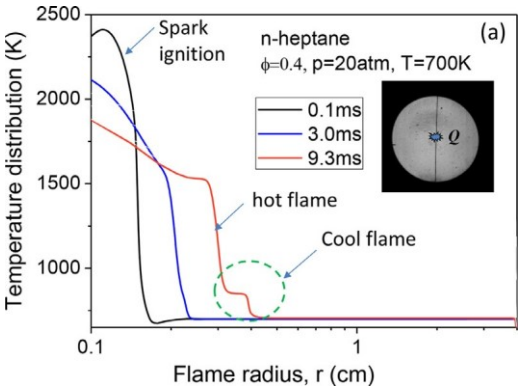

Fig. 17. Time dependent temperature distributions of an outwardly propagating double flame initiated by a hot spot at r = 0 cm an n-heptane/air mixture at 700 K, 20 atm, and equivalence ratio of 0.4 [29]. The kinetic model was reduced from [29,161].

To establish a planar cool flame, in 1950s, a flat flame burner [158] (Fig. 14a) was used to study the stabilization limits of cool flame and the two-stage warm flame of ether mixtures [40,41,47]. As shown in Fig. 14b, the cool flame and the two-stage warm flame only existed beyond the fuel rich limit of the hot flame. However, the cool flame had a much broader flammability limit than the two-stage blue flame on the fuel rich side. These results are consistent to the observation of the spontaneous ignition limits for cool flames and blue flames of n-butane/oxygen/nitrogen mixtures by Williams et al. [24–26] (Fig. 8). In 1970–90 s, more cool flame studies were carried out to measure the flame structures and speciation of fuel rich ethers, n-alkanes, di-t–butyl peroxide, and primary reference fuel (PRF) mixtures [41,43,149]. These studies advanced the understanding of flame structures and kinetics of fuel rich cool flames and warm flames.

It was until year 2000, an outwardly propagating spherical cool flame was first observed in microgravity by Foster and Pearlman [55–58] using fuel-rich butane/oxygen flames aboard NASA's KC-135 aircraft. Figure 15 shows the time sequence of the cool flame development after auto-ignition at the center of the vessel in a preheated mixture of 66.7% C_4H_{10} and 33.3% O_2 at initial pressure of 54.4 psi and 310 °C. Figure 16 shows the pressure time histories of the microgravity (μg) and normal gravity (1 g) cool flame development for the same mixture at an initial pressure of 4.4 psi [57]. It is seen that in microgravity, a two-stage pressure rise from cool flame to hot flame was observed. The effect of gravity on cool flame dynamics was also studied by using reduced gravity [58]. However, no microgravity experiments were conducted at fuel lean conditions and the measurements of cool flame speeds were not attempted either. Numerical modeling of the microgravity spherical cool flames was carried out by Fairlie et al. [159,160]. The results showed that the wall heat loss and preferential diffusion effects affected the cool flame propagation and quenching.

To understand low temperature combustion in fuel lean mixtures for advanced engine conditions, in 2010, Ju et al. [29] conducted numerical modeling of spark-assisted flame propagation of n-heptane/air mixtures at equivalence ratio of 0.4 (slightly above the lean burn limit of the hot flame) and pressure of 20 atm and initial temperature of 700 K. As shown in Fig. 17, immediately after a hot spot ignition at the center of the mixture (r≅0 cm), an outwardly propagating high-temperature flame was initiated (0.1–3.0 ms). However, at t = 9.3 ms, it

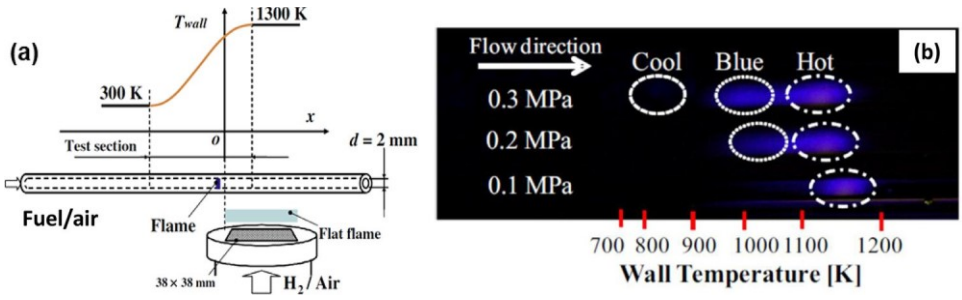

Fig. 18. (a) Schematic of the micro-reactor, and (b) Multi-stage flame images taken at P = 0.1–0.3 MPa for stoichiometric *n*-butane/air mixtures in the micro-reactor [69].

is seen that the hot flame front split into a two-stage double flame front, a leading cool flame with peak flame temperature around 820 K and a trailing hot flame with temperature above 1500 K. With a further increase in time, the leading cool flame propagates even faster than the trailing hot flame until the occurrence of the LTI in the region in the front of the cool flame. The computed cool flame propagation speed was about 27.5 cm/s. Although the numerical modeling showed that a premixed cool flame can propagate in a fuel lean mixture under engine conditions, it was not clear whether such a double flame structure above the lean flammability limit of hot flame is only a transient phenomenon or can be stabilized in the laboratory, and why the speed of a hot flame is slower than a cool flame.

To establish stable low temperature flames in laboratory and to study the flame structure, in 2010, Maruta et al. [65] investigated the stoichiometric dimethyl-ether/air combustion in a micro-reactor (Fig. 18a) by creating a temperature gradient of the reactor wall in the flow direction using external hydrogen flame heating. They observed that a three-stage premixed flame was stabilized by varying the flow velocity and the wall temperature gradient in the reactor. This study suggests that like the studies of Williams and Sheinson [25,26] for fuel rich mixtures, a multi-stage low temperature flame can be stabilized for a stoichiometric mixture by imposing a temperature gradient or using thermal management. This work was further extended to other fuels such as alkanes, isoalkanes, aromatics, and Primary Reference Fuels (PRFs) and other blended fuels at stoichiometric conditions and elevated pressures [65–69,162–164]. Figure 18b shows the dependence of the three-stage cool, blue, and hot flames on pressure. It is seen that with the increase in pressure, the cool flame and blue flame intensities increased and the flame stabilization location moved upstream. This study clearly showed that the formation of cool flames and multi-stage flames is sensitive to pressure and fuel reactivity in the micro reactor. Recently, Hori et al. [67,165] extended the multi-stage flame studies in the micro reactor to define a fuel reactivity index for gasoline fuels. Moreover, to understand the effect of the reactor wall reactivity on cool flames, various metals, metal oxides, and quartz surfaces were used to understand the radical quenching on dimethyl ether/air cool flames [68,90,166]. The results showed that a metal wall may exert strong influence on the low-temperature oxidation via catalytic reactions or radical quenching. Nevertheless, most of the studies in micro combustor were conducted at stoichiometric conditions with external wall heating. It was not clear whether a self-propagating cool flame can be observed in a fuel lean mixture without a fixed temperature gradient created by wall heating.

To understand the dynamics of self-sustaining, planar, and unstretched premixed cool flames in fuel lean mixtures, Ju et al. [167,168] conducted numerical simulations of one dimensional freely-propagating DME-oxygen flames [169]. Figure 19 shows a schematic of the computed flame temperature dependence on the equivalence ratio, respectively, at 1 and 20 atm. Similar to the observation in Fig. 14, it is seen that the numerical modeling well-captured the existence of multi-staged flames and cool flames on fuel rich mixtures beyond the hot flame's rich flammability limit. Moreover, it is also predicted that there exists a lean cool flame below the lean flammability limit of the hot flame. Furthermore, at a lower pressure (1–4 atm), the transition from the hot flame to multi-stage flames and cool flames on the rich side is a smooth transition without a hot flame extinction. However, the transition from a hot flame to cool flame on the fuel lean side shows an extinction-ignition S-curve. Because of this, it is seen that in a broad equivalence ratio range on the fuel lean side, three different flame regimes, cool flame, double flame, and hot flame, can all exist. The double flame on the S-curve shown in Fig. 19 is not on the stable flame branch. A small perturbation will trigger the double flame to transfer to either a hot flame or a cool flame. However, as will be shown later, with radical loss and heat loss in a counterflow flame [84,98] or in an unsteady spherical flame propaga-

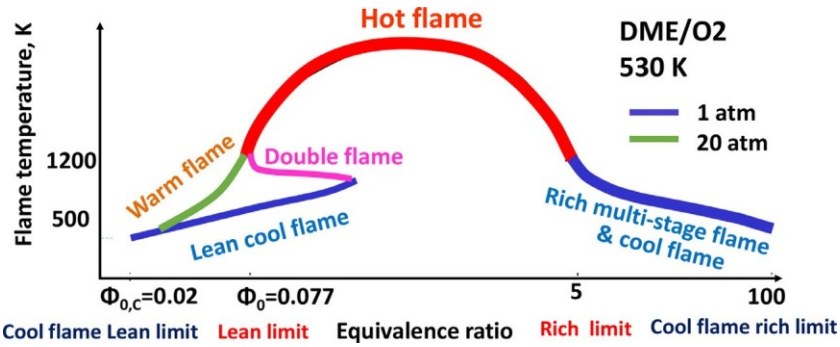

Fig. 19. Schematic of computed flame temperatures and flammability limits of planar freely-propagating hot flames, cool flames, and warm flames of DME/O_2 mixtures at 1 and 20 atm. $_{0,C}$: the lean limit of the cool flame, $_{0,}$: the lean limit of the hot flame [167]. The DME kinetic model was taken from [145,167].

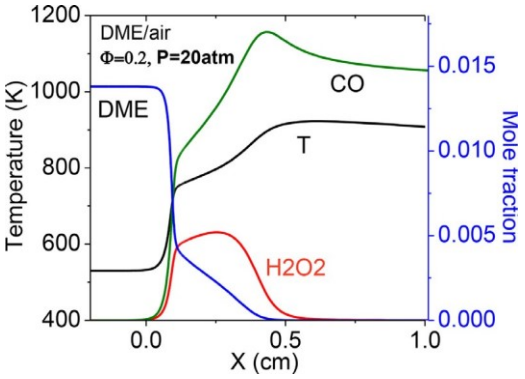

Fig. 20. The simulated flame structure of high-pressure lean cool flame for a DME/air mixture at = 0.2 and P = 20 atm [168]. The ozone and DME kinetic models were from [145,167].

tion (Fig. 17) [29,99,106], a stable or quasi-steady double flame propagation can be observed. With the increase of pressure (above 5 atm), it is interesting to note that similar to the fuel rich side, the transition between the hot flame and cool flame on the fuel lean side also becomes monotonic due to the appearance of a warm flame. This prediction of a smooth transition from hot flame to warm flame for fuel lean mixtures remains to be experimentally validated at elevated pressure.

The simulated flame structure of a warm flame at equivalence ratio of 0.2 at 20 atm is shown in Fig. 20. It is seen that the lean warm flame has a two-stage flame structure which consists of a leading cool flame front at x = 0.1 cm and a trailing intermediate temperature flame front at x = 0.3 cm (Fig. 20). Note that a self-sustaining lean warm flame only exists below the lean flammability limit of the hot flame. Moreover, different from the leading cool flame, the trailing flame front at the intermediate temperature of the warm flame is an auto-ignition assisted flame front. The multi-stage flames shown in Fig. 18 at stoichiometric condition existed because of the superimposed temperature gradient by the heated reactor wall. This flame cannot propagate without the external heating. At high pressure, when the mixture is slightly below the hot flame lean limit, the HO_2 chemistry (Table 3) becomes so strong that the heat release from the leading cool flame is sufficient to trigger an ITI downstream to form a warm flame. Therefore, at high pressure, the warm flame is a bridge between the cool flame and the hot flame on both fuel lean and rich sides and results in a smooth transition between them.

From the numerical modeling, the flame regime boundaries and burning limits of lean premixed cool, warm, and hot flames as well as the double flames can be plotted in Fig. 21. Line BAB' is the lean burn limit of the hot flame. Therefore, hot flames only exist on the right hand side of line BAB' (regions I and II). Line DE is the lean burn limit of cool flames and line A'AC is the upper limit or the reignition limit of cool flames of the fuel lean cool flames. On the reignition limit (A'AC), the cool flame reignites and becomes a hot flame (see Fig. 19). As such, cool flames only exist between lines DE and A'AC in the regions of II and III. Therefore, in region II, where the hot flame and cool flame regimes overlap, one can observe either a hot flame, a cool flame, or even a double flame, depending on the initial conditions. At high pressure, the warm flame starts to appear in region IV in the region between lines AA' and AB'. With a further increase of pressure, the transition from cool flame to warm flame (line A'A) occurs at a lower equivalence ratio due to the enhancement of the HO_2 chemistry. However, the transition from warm flame to hot flame is much less sensitive to pressure because of the stronger temperature dependency of the chain-branching reaction of a hot flame in Eq. (3). The transition between the cool flame and warm flame as well as the hot flame at high pressure

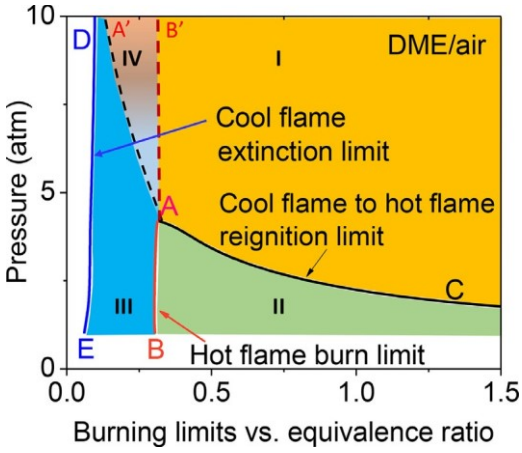

Fig. 21. A flammability limit diagram for cool, warm, and hot flames at elevated pressure. Region I: hot flame; Region II: either a hot flame, a double flame, or a cool flame, Region III: cool flame, and Region IV: warm flame. AA' is the boundary between the cool flame and warm flame, and AB' is the boundary between warm flame and hot flame. [168]. The ozone and DME kinetic models were from [145,167].

is a smooth transition for fuel lean mixtures. Therefore, understanding the burning limits of different flame regimes and the transitions helps to understand the dynamics of cool flame, warm flame, and hot flame in experiments and modeling and to develop new experimental methods to study them.

To experimentally observe the self-stabilized lean premixed cool flames, Reuter et al. [84] and Zhao et al. [170] conducted the counterflow experiments for DME/oxygen mixtures with and without ozone addition (Fig. 22). Ozone plays a role to sensitize the LTC of DME to enable cool flame stabilization at low inert N_2 temperature. Moreover, if the inert N_2 temperature is raised high enough, an auto-ignition assisted premixed cool flame can be sustained without ozone [170]. Figure 22 shows a schematic representation of the experimental setup of Reuter et al. [84]. Here only a brief description is provided. Details of the experiments can be found in [83,84,171–174]. The upper burner nozzle issues pure nitrogen heated up to 600 K. The lower oxidizer stream initially consists of pure oxygen at 300 K, which passes through a non-equilibrium plasma ozone generator to produce ozone. The burner separation distance was set to 2.25 cm. The strain rate (a) is defined as the density-weighted gradient of the axial flow velocities on the oxidizer side. PLIF was used for CH_2O detection [171–173,175,176]. Direct images of a DME/O_2/O_3 premixed cool flame and hot flame at the same conditions of ϕ=0.14 and a =89 s^{-1} are shown in Fig. 22(a) and (b). The cool flame was observed to be visibly dimmer than the hot flame. CH_2O PLIF images showed that cool flame had a very high concentration of CH_2O formed through LTC. However, CH_2O in the hot flame was low and limited only to the thin zone in front of the high-temperature flame zone. Figure 22(c) shows a double flame image at a =59 s^{-1} and ϕ=0.087 [98], in which the lower dimmer zone is a premixed cool flame and upper brighter zone is a hot flame.

Reuter et al. [98] further measured the cool flame extinction (CFE) limit, the hot flame extinction (HFE) limit, and the structure of near-limit hot flames. As shown in Fig. 23, with the decrease of equivalence ratio, the extinction limit of hot flame became smaller than the cool flame. This result indicates that a cool flame can burn at the sub-limit condition of a hot flame. This result supports the schematics in Figs.19 and 21. Note that when the equivalence ratio is slightly above the hot flame flammability limit, a stable near-limit double flame appears (inset image in Fig. 23). Note that as shown in Fig. 19, an unstretched planar double flame is not stable. However, in a counterflow flame, the heat and radical losses due to the finite flow residence time could stabilize a double flame. Also, note that a double flame is different from a warm flame. The former is a two-stage flame governed by LTC and HTC and can exist only above the hot flame lean flammability limit (Region II in Fig. 21). The latter is a two-stage flame governed by LTC and ITC chain-branching reaction pathways (Eqs. (1)-(2)) and can exist only below the lean hot flame flammability limit (Region IV in Fig. 21) or above the rich hot flame burning limit.

Therefore, by using an atmospheric counterflow flame, one can observe all three premixed flame regimes: cool flame, hot flame, and double flame shown in Figs.19 and 21. If one raises the pressure, as the ITC chain-branching reaction pathway becomes faster, a stable warm flame could be observed as well. In addition, since the double flame occurs at similar conditions of cool flame, if the double flame is perturbed by a flow vortex or fuel dilution, a transition between double flame and cool flame can be observed. Figure 24 shows the time history of CH_2O PLIFs of a double flame affected by an impinging vortex from the top. It can clearly be seen the transition from a double flame in Fig. 24(a) (thinner CH_2O zone) to a double flame local extinction in Fig. 24(b), a formation of cool flame next to the double flame (with thicker CH_2O zone) in Fig. 24(c), and the extinction of the cool flame in Fig. 24(d) and (e). Therefore, in low temperature combustion, all different flame regimes and their transient transitions can occur.

To measure the flame speed of a premixed cool flame, a weakly stretched planar premixed DME cool flame was established by Hajilou et al. [97] using a Hencken burner [178] at low pressure (7.3 kPa) with ozone sensitization (Fig. 25a). At low enough pressures, as shown in the inset image in Fig. 25b, with the increase of flow rate, a transition from a burner-stabilized cool flame mode to a

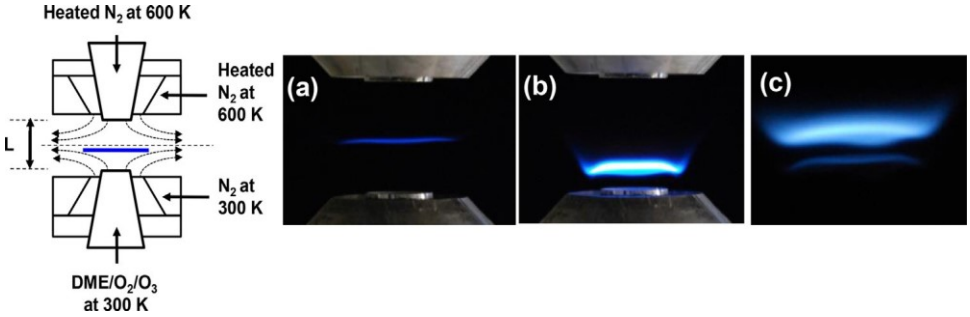

Fig. 22. (Left) Schematic of the ozone-assisted counterflow burner. (Right) (a) Direct image of cool flame and (b) a hot flame image at = 0.114 and a strain rate of $a = 89\ s^{-1}$ [84]; (c) a double flame image at $a = 59\ s^{-1}$ and = 0.087 [98].

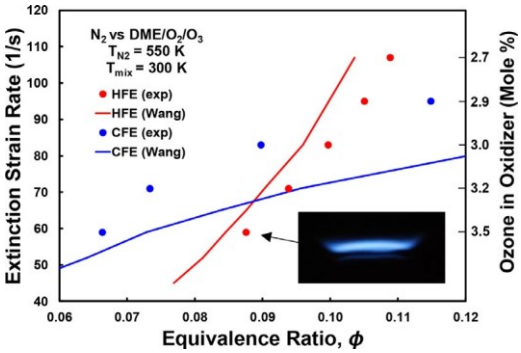

Fig. 23. Measured and computed extinction limits for DME/O_2/O_3 cool flames and hot flames. The inset image shows a near-limit double flame at $a = 59\ s^{-1}$ and = 0.087 [98]. The kinetic model was from [177].

freely-propagating cool flame mode occurs [97]. By using the flow rate at the transition point between the two flame modes, the laminar cool flame speeds of DME were measured from 0.4 to 1.4. However, cool flame speeds at high pressure have not been successfully measured due to their low flame speed. Future studies need to address this issue.

3.2. Non-premixed cool flames and warm flames

3.2.1. Droplet cool flames and warm flames

In 2012, a major progress was made in the observation of diffusion cool flames in microgravity droplet combustion conducted in the FLEX program [79]. It was found that a large *n*-heptane droplet exhibited dual modes of combustion, the high temperature diffusion flame and a low temperature cool flame. Figure 26 shows the dependence of the square of the droplet diameter and the flame size on the time after ignition at three free-floating droplet burning conditions. It is seen that right after the hot flame ignition at t=0 s, the typical quasi-linear relation between the square of the droplet diameter and time of a high temperature droplet combustion was observed. However, after the hot flame extinction with a rapid drop of flame luminescence, the rate of droplet size decrease was unchanged until 35, 26, or 13 s, respectively, depending on the initial droplet size. To explain the abnormal phenomenon, it was suggested that the continued droplet burning after the radiative extinction of the hot flame was a cool flame [79,80].

Numerical simulations of microgravity droplet cool flame burning were conducted extensively by Farouk et al. [70–72,116,179] for different fuels such as alkanes and PRFs with different diluents. The effects of cool flame chemistry and molecular diffusion on droplet cool flame formation and the oscillatory cool flame re-ignition were exam-

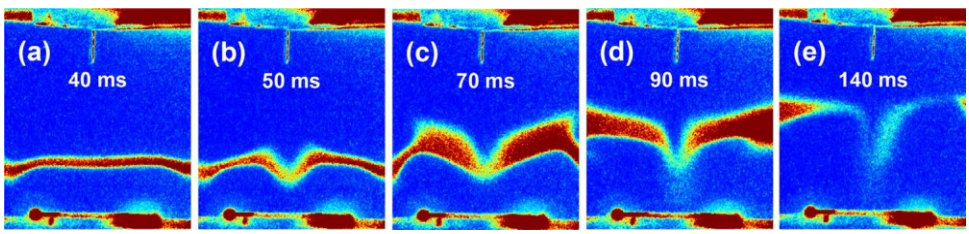

Fig. 24. CH_2O PLIF sequence showing the impact of an impinging vortex on a counterflow double flame at strain rate of $a = 75\ s^{-1}$. The vortex velocity is approximately 13.6 m/s [98].

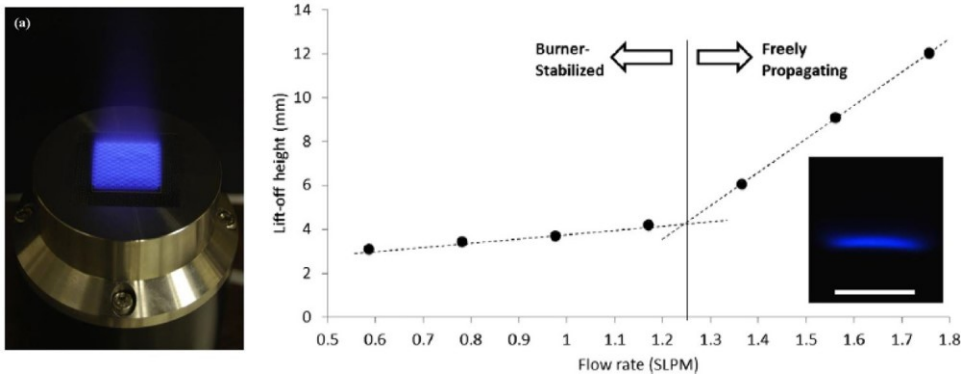

Fig. 25. (a) Image of a Hencken burner under operation, (b) Lift-off heights for DME/O_2/O_3 cool flames (0.6, 7.3 kPa) over a range of reactant flow rates, showing burner-stabilized and freely-propagating flame regimes [97].

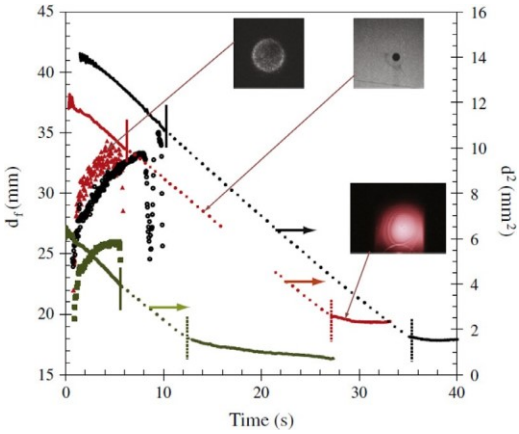

Fig. 26. Three representative examples of radiative extinction and subsequent second-stage combustion of *n*-heptane droplets with different droplet diameters, showing the flame diameter (d_f) and the square of the droplet radius (d^2) as a function of time. Vertical solid lines denote the end of OH* emissions, and vertical dotted lines denote the second-stage extinction. The insets are a representative UV camera flame image taken during the hot-flame stage (top), a backlit droplet image during the second stage (middle), and a fuel vapor cloud image subsequent to the second extinction (bottom) at the transition point [79].

ined. Figure 27 shows the predicted time histories of *n*-heptane droplet diameter, burning rate, flame diameter and peak gas temperature, respectively, with and without including LTC in the chemical kinetic models [161,180] in comparison with the experimental data [70]. It is seen that only the kinetic model with LTC could capture the second-stage cool flame burning mode. Nevertheless, it was also shown that there were significant discrepancies between the measured and computed cool flame extinction diameters due to the uncertainties of LTC due to the lack of validation data of cool flames.

To understand the cool flame chemistry and dynamics, theoretical analyses of droplet cool flames of different n-alkanes of varying initial droplet size in oxygen/nitrogen, oxygen/nitrogen/carbon dioxide, and oxygen/nitrogen/helium environments at different pressures were analyzed by Nayagam and Williams using the large activation energy theory with simplified skeletal mechanisms [76–78,118,119]. A similarity trend between cool-flame extinction diameters (D_{CE}) normalized by the burning-rate constant K_c for all three n-alkane droplets were shown to follow a similar trend as functions of the oxygen concentration (Fig. 28). More recently, by using Liñán's partial-burning regime, prediction of droplet cool flame burning-rate constants and flame standoff ratios for n-alkane fuels was made. Comparisons with experimental results showed an improved rate-parameter estimate for n-dodecane. However, the prediction by the simplified chemistry had an increased discrepancy with experiments with increasing pressure for droplet diameters at cool-flame extinction. Some reaction rate adjustment was needed to improve the prediction.

Recently, microgravity cool flame experiments were further extended to bi-component droplets of decane and hexanol at higher pressures [75]. The results revealed that at some conditions, the transition from radiative extinction of the hot flame to the cool flame has oscillatory multicycle reignition where the flame undergoes multiple hot-cool flame transitions [71]. The results also showed that, depending on the ignition energy, there exists a direct ignition to cool flame transition without radiative extinction of a hot flame when the ignition source is carefully controlled [72,181]. The bi-component decane and hexanol experiments [75] showed even more intriguing cool flame extinction and reignition phenomena at elevated pressure. At 0.20 MPa, the results showed that the large fiber-supported hot flame radiatively extinguished and then became a cool flame for a period of time before the

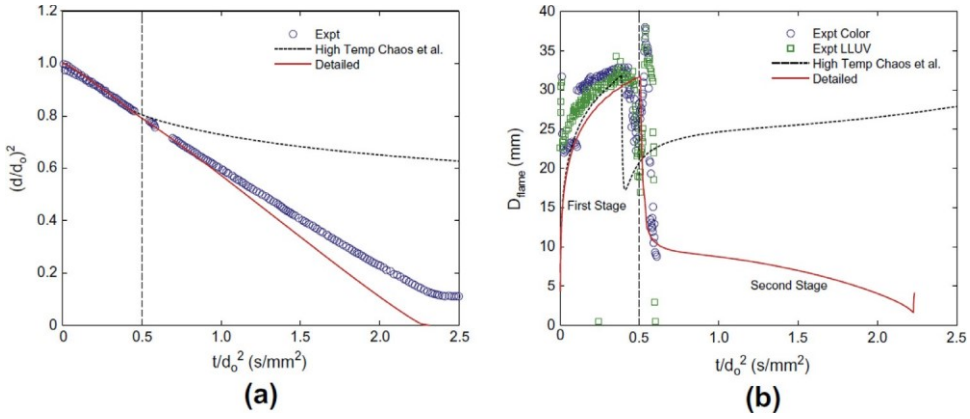

Fig. 27. Measured and predicted evolutions of (a) droplet diameter, (b) burning rate for a *n*-heptane droplet in ambient air (d_o ≈3.91 mm, 0.21 X_{O2}, 0.79 X_{N2}, P ≈1 atm) [70]. Predictions were made using a detailed *n*-heptane model [161] and a high-temperature *n*-heptane model [180], respectively.

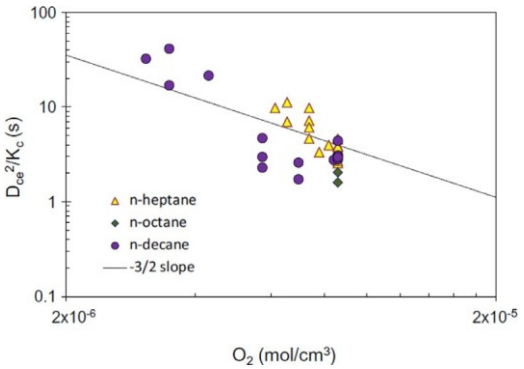

Fig. 28. Cool-flame residence time at extinction as a function of ambient oxygen molar concentration for n-alkane droplets in $O_2/CO_2/N_2$ environments [76].

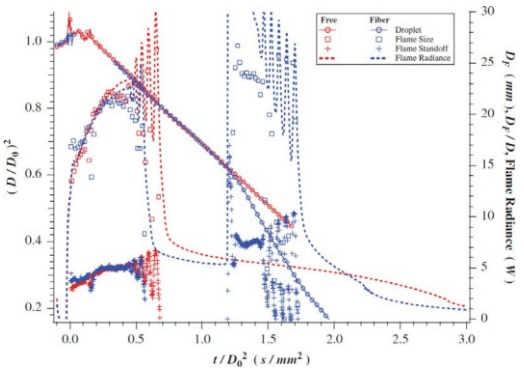

Fig. 29. Comparison of droplet, flame, and radiance histories between a free-floated and fiber-supported decane-hexanol (50–50 by volume) droplet in a 0.20 MPa. The initial droplet sizes for the two droplets were 4.5 mm (free-floated) and 4.4 mm (fiber-supported). The reignition of the fiber-supported droplet is clear in the flame radiance data. The data recording stopped before the test was complete, but the color camera data coupled with the flame radiance data showed the droplet burned to near completion [75].

cool flame re-ignited to a hot flame. At 0.30 MPa, the hot flame again radiatively extinguished and burned with a cool flame without the cool flame reignition to a hot flame phenomenon. The droplet burned to completion with a cool flame. Figure 29 shows the effect of droplet suspension (fiber vs. free floated) on the cool flame reignition at 0.20 MPa. The experiments highlighted the fact that the fiber-supported droplets undergo cool flame reignition but the free floated droplets do not. The pressure and suspension dependent cool flame dynamics raised some concerns of the reliability of cool flame chemistry. Farouk and Dryer [182,183] later reported that the presence of a tether could also be a significant source of thermal perturbation especially through the feedback to the droplet.

More recently, FLEX 1268 experiment [74] of *n*-dodecane droplet burning at elevated pressure (~2.7 atm) in air diluted with helium revealed that there was a transient three-stage (hot flame, warm flame, and cool flame) burning behavior (Fig. 30). The computational and experimental results showed that the diffusion heat transfer, enhanced by helium substitution, extended the second-stage warm flame burning mode until the heat loss became too large. Therefore, both chemistry and transport process affect the dynamics of cool flames and warm flames.

3.2.2. *Counterflow cool flames and warm flames*

Since 2013, self-sustaining non-premixed cool flames have been successfully established in the counterflow configuration at Princeton with and without plasma and ozone sensitization [82,83,92].

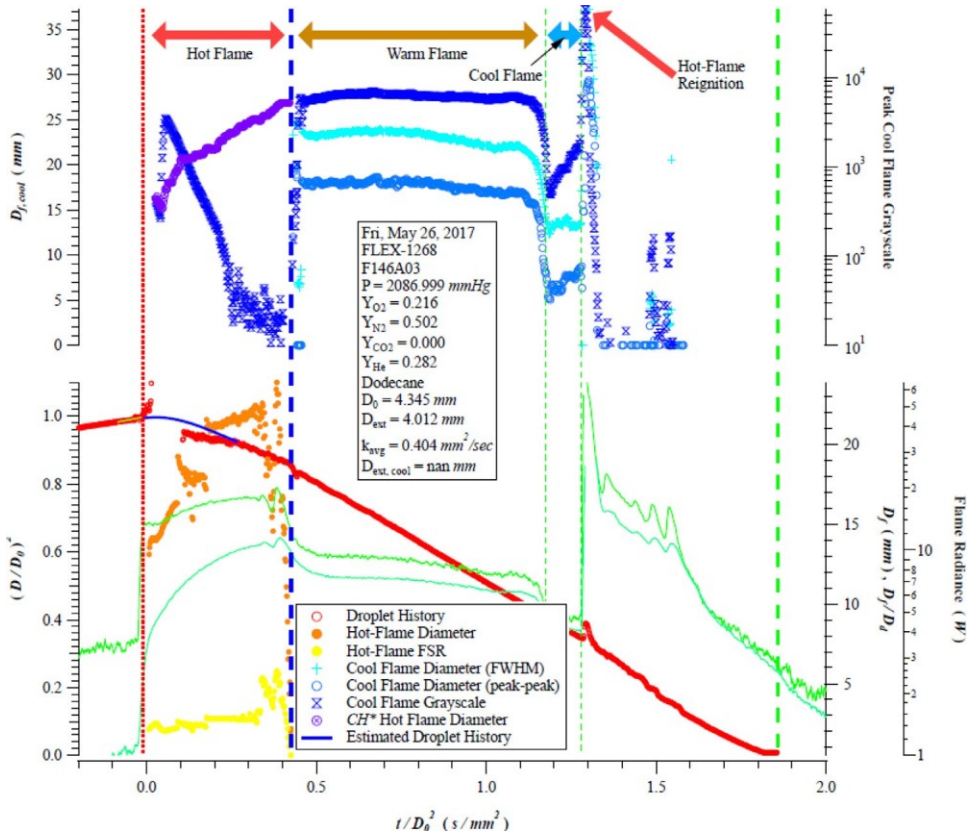

Fig. 30. Measured evolution of droplet diameter, flame diameter, and radiant heat for an *n*-dodecane droplet combustion (d_o = 4.35 mm, 2.75 atm, Y_{O2} = 21.6%, Y_{He} = 28.2% and balance N_2, FLEX 1268) [74].

Early studies on non-premixed counterflow cool flames began with numerical modeling of the NTC effect on ignition limit [64,184]. Law and Zhao [64,111] computationally studied the NTC effect on the ignition and extinction of *n*-heptane/air in the non-premixed counterflow configuration. Fig. 31 shows the NTC effect on the ignition S-curve. It is seen that the ignition S-curve at low strain rates has an additional cool flame branch. Moreover, the critical strain rate for NTC effect increased with the increase of pressure.

By using plasma and ozone to sensitize the low-temperature fuel reactivity [83,96], Won et al. [83] successfully stabilized a self-sustaining *n*-heptane/O_2 non-premixed cool flame in a counterflow burner. Figs. 32(a) and (b) show the comparison between a cool flame and a hot flame at the same boundary conditions. Since ozone molecules begin to decompose into O radicals around 450 K, as seen in Figs.11–12 and 36, O radical addition will accelerate LTC and enable cool flame formation at a shorter flow residence time. Numerical calculations (Fig. 32b) [83] showed that there existed two flame regimes (cool and hot) at the same conditions. The addition of 3% ozone in oxygen extended the

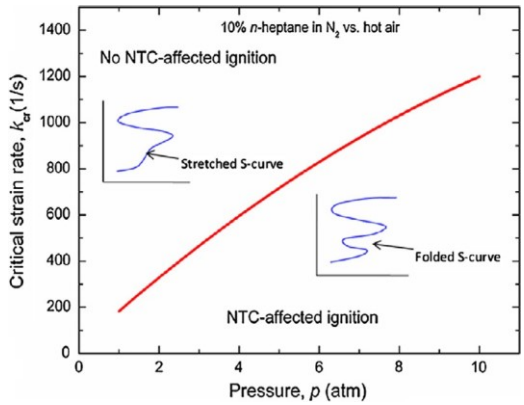

Fig. 31. Calculated regime boundary of NTC-affected ignition in a non-premixed counterflow of 10% *n*-heptane in N_2 [59,111] with a reduced kinetic model in [59].

CFE limit from a_g=46 s^{-1} to 141 s^{-1}. As reported by Reuter et al. [86], a self-sustaining cool flame could be sustained even after removing the ozone at a strain rate within the CFE limit.

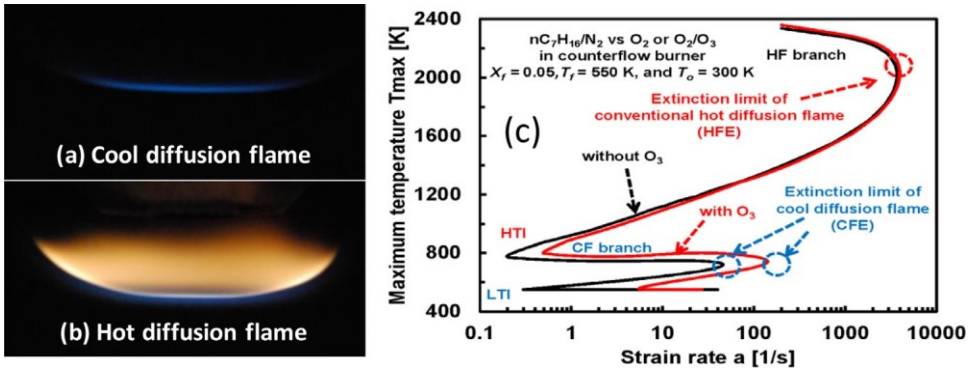

Fig. 32. (a) Direct photo of atmospheric non-premixed cool flame for an *n*-heptane/O_2–O_3 mixture of $X_f = 0.07$, $a = 100\ s^{-1}$, and 3% O_3; (b) Direct photo of the hot flame observed at identical conditions [83]. (c) Calculated S-curves [161] in the same counterflow configuration for X_f 0.05 with and without 3% ozone addition at the oxidizer side [83] with the kinetic model in reduced version of [161].

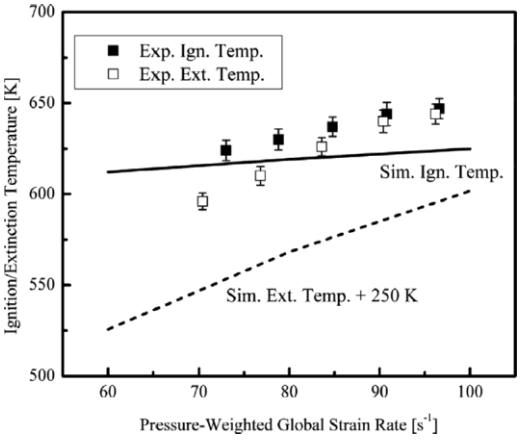

Fig. 33. Experimental and computed (with kinetic model in [145]) ignition and extinction temperatures at 2 atm and various strain rates. The computed extinction temperature is shifted up by 250 K for better illustration. DME volume fraction in the fuel stream is 50%, and the oxidizer stream is air [95].

Deng et al. [92] conducted experimental studies on the hysteretic ignition and extinction behavior of the non-premixed DME/air cool flame at both atmospheric and elevated pressures [92,95]. The hysteretic ignition and extinction behaviors of the non-premixed cool flame were observed. The results showed that significant discrepancies existed for the extinction temperatures even with the well-adopted reaction mechanism (Fig. 33). Possible reasons for the discrepancy was found to be in the uncertainty of the branching ratio of QOOH decomposition and oxygen addition (Fig. 12). It was shown that by adjusting this branching ratio, the agreement between experiment and prediction was improved (Fig. 33). This outcome is also consistent with the finding in a flow reactor experiment [185]. Therefore, the availability of cool flame data provides a critical validation target to LTC.

More recently, Yehia et al. [186] conducted atmospheric non-premixed warm flame experiments using dibutyl ether/oxygen-ozone in a counterflow burner (Fig. 34). They observed a self-sustaining low-temperature non-premixed warm flame, existing between the cool flame and hot flame. Fig. 34 (left) shows a direct image of a two-stage dibutyl ether warm flame. The warm flame has two reaction zones, a cool flame on the fuel side (top burner) and an intermediate-temperature flame on the oxidizer side (bottom burner). Fig. 34 (right) shows the computed species mole fractions and heat release rate distribution. It is clearly seen that there are two heat release zones. The heat release rate and OH concentration in the ITC reaction zone are higher than that in the LTC reaction zone. The cool flame on the fuel side was formed by the oxygen leakage from the ITC reaction zone. The ITC reaction zone for warm flame on the right is formed via the fuel fragments from the cool flame at a higher oxygen concentration on the oxygen side. Numerical analysis showed that different from the cool flames, the most important elementary reactions for the warm flames are the HO_2 chemistry and the ITC chain-branching reactions in Table 3. Yehia et al. [101] also observed the two-stage non-premixed warm flame formation for *n*-alkanes in an atmospheric counterflow burner. However, the prediction and experiment have large discrepancy in the transition limits between cool flames and warm flames. The uncertainty of HO_2 chemistry for warm flame needs to be addressed in the future.

To understand the flame dynamics of non-premixed cool flames and warm flames and their

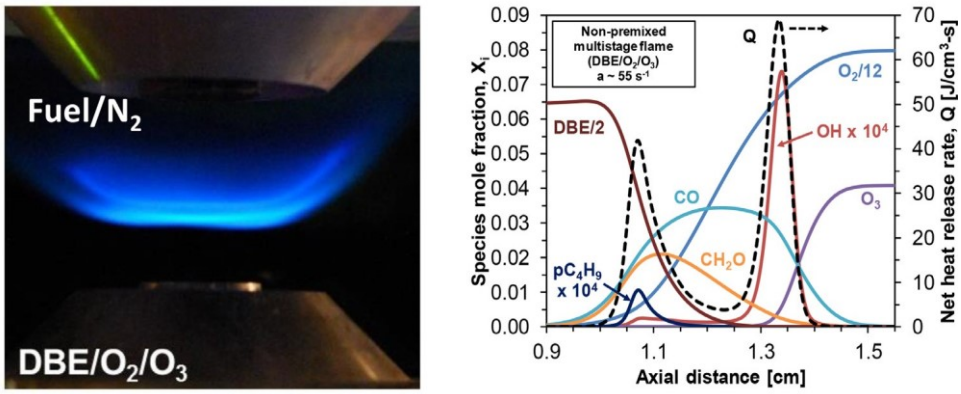

Fig. 34. Left: Direct image of multi-stage non-premixed warm flame of dibutyl ether/oxygen-ozone in a counterflow configuration [186]. Right: Simulated species mole fraction and chemical heat release rate distributions with a kinetic model of [187].

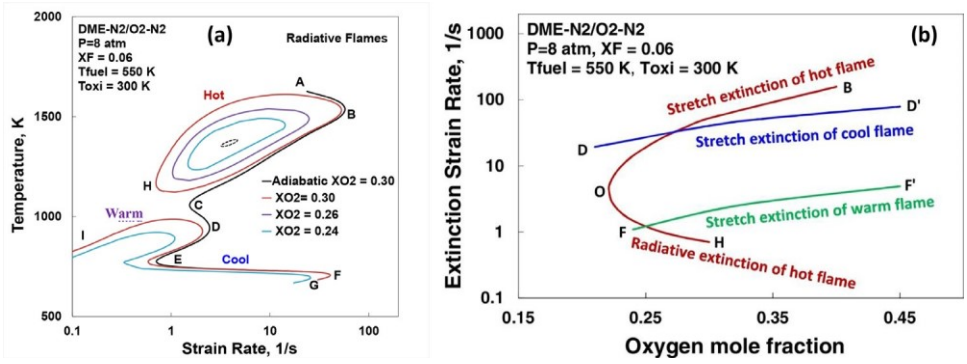

Fig. 35. Calculated (model from [139]) dependence of flame temperature on the stretch rate of non-adiabatic DME-N_2/O_2–N_2 non-premixed flames for different oxygen mole fractions of 0.3, 0.26, and 0.24 at 8 atm [113]. (b) Predicted flammability limit diagram for non-premixed cool, warm, and hot flame regimes as a function of oxygen mole fraction for DME-N_2/O_2–N_2 non-premixed flame [113].

relationship with hot flame burning limits. Lin et al. [113] simulated near-limit DME/O_2 diffusion flames at different pressures, temperatures, and oxygen and fuel concentrations with and without radiation heat loss. Figure 35a shows that the flame temperature dependence on the strain rate for hot flame, cool flame, and warm flame with the decrease of oxygen mole fraction (X_{O2}) in the oxidizer stream. For the adiabatic flame at X_{O2} 0.3, there exist three different flame branches (hot flame AB, warm flame CD, and cool flame EF). When radiative heat loss is considered, the hot flame branch and the low temperature flame branch are separated. The hot flame is bounded by a radiative extinction limit at a lower strain rate (H) and a stretch extinction limit at a higher strain rate (B). As the X_{O2} decreases the hot flame flammable region narrows and there is a flammability limit near X_{O2} 0.23. However, the cool flame burning limit is much less affected by the oxygen mole fraction, and the warm flame (ID) can be observed in a broad region of low stretch rates. Figure 35a clearly reveals the relationship between the near-limit three non-premixed flame regimes. Figure 35b plots the flammability limit diagram for all three non-premixed hot, warm, and cool flame regimes in the phase space of strain rate and oxygen mole fraction. The C-shaped curve (BOH) represents the stretch and radiative extinction limits (points B and H, respectively, in Fig. 35a) of the hot non-premixed flames. The DD' line in Fig. 35b represents the stretch extinction limit of the cool flame. The FF' line denotes the stretch extinction limit of the warm flame. Therefore, Figure 35b provides qualitative guidance for experiments to observe different kinds of flame regimes. Note that the increase in pressure, fuel concentration, and reactant temperatures will modify the flammable boundaries of cool and warm flames in Fig. 35b [113].

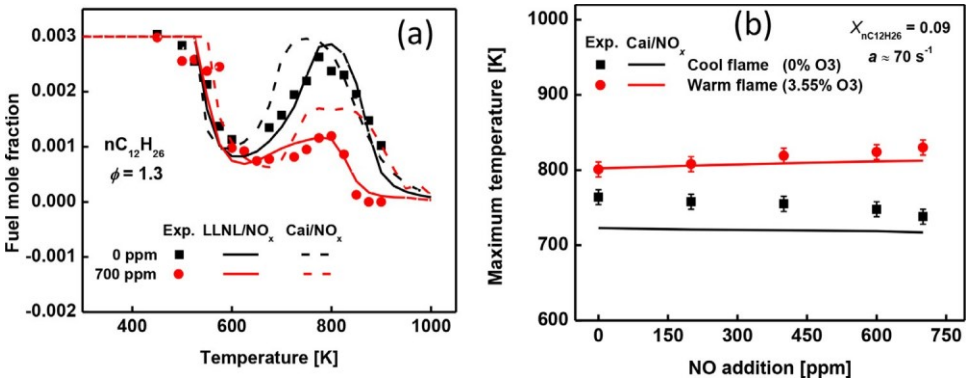

Fig. 36. (a) Predicted and measured temperature evolutions of the mole fraction of *n*-dodecane at fuel rich condition without and with 700 ppm NO addition in a jet stirred reactor. (b) Measured maximum temperatures of *n*-dodecane flame with various NO additions [102]. Kinetic model was from [102].

3.3. Control of cool flames and warm flames using chemical sensitization

As discussed above, ozone is a good chemical sensitizer to promote LTC and ITC for cool flame and warm flame formation. Other methods such as plasma discharge [96,188], NO_x [189-194], and ethers or diesel sensitizers [100,195,196] also provide an effective way to control cool flame and warm flame formation. A recent experimental study of the NO effect on n-dodecane non-premixed cool flames and warm flames by Zhou et al. (Fig. 36) [102] shows that NO has a distinctive impact on cool flame and warm flame, respectively, via the alkyl peroxy radical termination reaction, $RO_2 + NO \rightleftarrows RO + NO_2$, at low temperature and the OH radical production from HO_2 via reaction $HO_2 + NO \rightleftarrows NO_2 + OH$ at intermediate temperature [189,191,193]. Figure 36a shows that 700 ppm NO addition to n-dodecane slightly delays LTC but significantly suppresses NTC and accelerates ITC in a jet stirred reactor experiment. Figure 36b shows that in a counterflow experiment, with the increase of NO addition, the cool flame temperature decreases while the warm flame temperature increases. This experiment clearly shows that NO addition suppresses cool flames but promotes warm flames. Therefore, low temperature combustion can be controlled via chemical sensitization. However, more experiments at high pressure are needed to understand this chemical sensitization effect at engine conditions due to strong HO_2 and NO chemistry coupling.

4. Auto-ignition assisted propagation of cool flames and warm flames

4.1. Auto-ignition assisted cool flames

In many practical engines, the inlet temperature is so high that the mixture is already in an auto-igniting environment. In addition, the mixture composition and temperature may not be uniform. Therefore, combustion in engines may also be affected by auto-ignition assisted flame propagation. By analyzing the laminar non-premixed flamelet equations under engine conditions with the observation from DNS [197,198] and experiments [34,199], Dahms et al. [114] summarized the likely ignition and combustion time evolution in an engine in Fig. 37. It is seen that low temperature ignition will occur first at fuel lean conditions and then followed by turbulent cool flame propagation into fuel rich mixtures. After that, a second-stage ignition occurs in a fuel rich mixture and triggers the HTI. Finally, the HIT will initiate hot flame formation which travels towards the near stoichiometric mixture location.

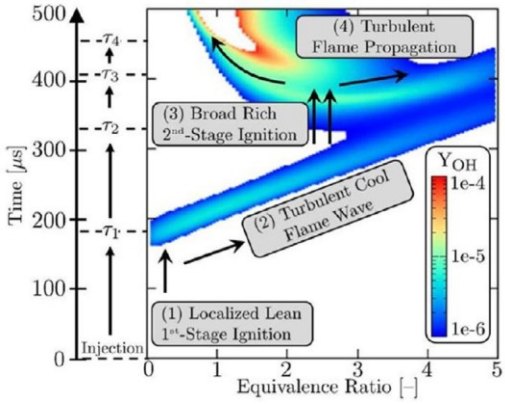

Fig. 37. Evolution of characteristic events and associated time scales for ignition in high-pressure spray flames [114].

To examine the effect of flame regimes under autoignitive conditions, Krisman et al. [109] studied the ignition, flame structure and propagation of

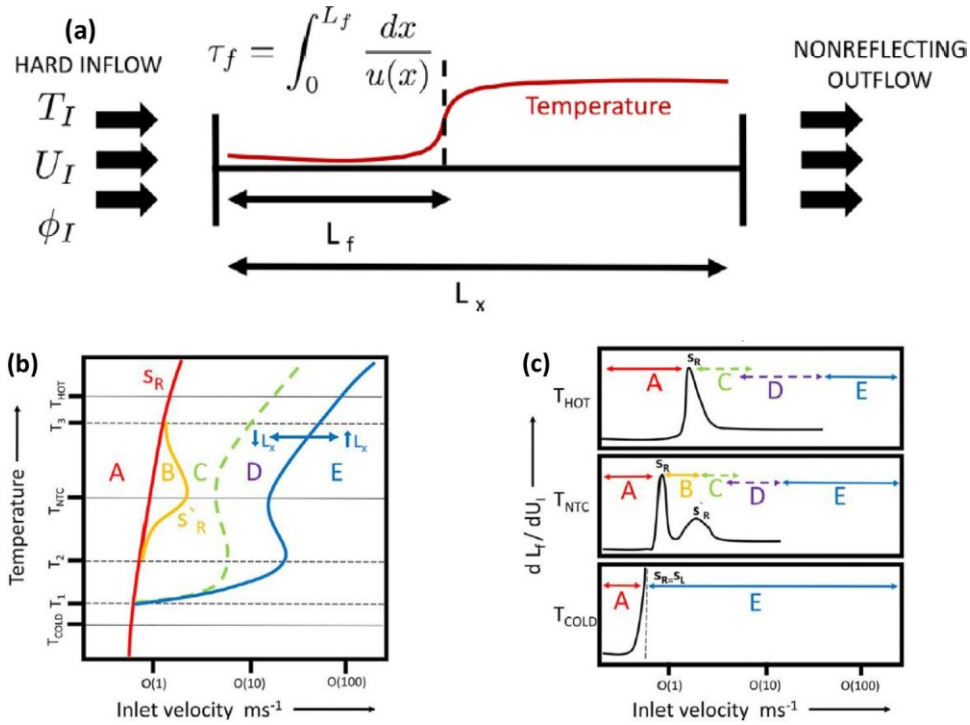

Fig. 38. (a) Schematic of the 1-D computational domain with length L_x. The left boundary is an inflow with a fixed velocity U_I, temperature T_I, and equivalence ratio Φ_I. The flame location L_f is defined by the location where the HRR is maximum. (b) A regime diagram for a 1-D premixed flame in temperature-velocity space for a hypothetical NTC fuel. (c) Evaluations of dL_f/dU_I with respect to U_I for temperatures T_{HOT} (upper), T_{NTC} (middle), and T_{COLD} (lower). The transitions in regime with respect to U_I and the laminar flame speeds are also shown [109].

a freely-propagating laminar flame in a fixed computational domain. Figure 38 shows the schematic of the computational domain and the dependence of the flame location and structure on the inlet flow velocity and temperatures. Figure 38b shows the computed flame regime diagram from [109] in temperature-velocity space. Regime A is the burner-stabilized flame regime by either auto-ignition or flame propagation at low inlet flow velocities. Regime B is the LTI-assisted flame propagation and only exists for fuel chemistry including LTC. Regime C is the auto-ignition assisted flame propagation which is significantly affected by the pre-ignition chemistry. Regime D is auto-ignition stabilization and no premixed flame structure exist. The transition from regime C to regime D was gradual. Blow-off occurred in regime E.

To understand how fast an auto-ignition assisted cool flame and warm flame can propagate at different temperatures and pressures, Zhang and Ju [91] simulated the propagation speeds of n-heptane/air cool and warm flames at elevated temperatures and pressures at large ignition Damköhler numbers (Table 2). Figure 39 shows the dependence of cool flame speed on initial temperature for a mixture, respectively, below ⩽0.2, regime III in Fig. 21) and above the hot flame flammability limit (⩾0.5, regime II in Fig. 21). It is seen that the sub-limit cool flame speed shown in Fig. 39a has a strong non-linear dependence on initial temperature due to the NTC effect. In addition, before the NTC transition, the cool flame speed is much higher than the hot flame speed. Even when the mixture is above the hot flame flammability limit, Fig. 39b shows that although the hot flame speed monotonically increases with the initial temperature, the cool flame speed remains a non-monotonic dependence on the initial temperature. Note that at a certain temperature range, the cool flame speed can still be faster than the hot flame speed. This explains the mechanism of the double flame structure formation shown in Fig. 17. Again, in the NTC region, the cool flame speed decreases rapidly. With a further increase of the initial temperature, the cool flame reignition occurs (the arrow in Fig. 39b) and transition to the hot flame. This is the cool flame reignition limit shown in Fig. 21. Therefore, the cool flame burning cannot be ignored for both sub-limit and above-limit combustion at elevated temperature and engine conditions.

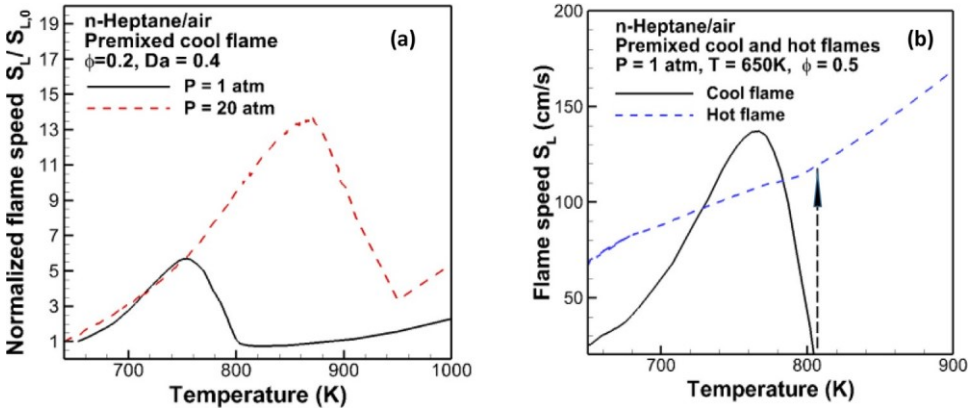

Fig. 39. The predicted relation between the normalized premixed cool flame speed and the initial temperature of n-heptane/air mixtures for, (a) lean cool flames below the hot flame flammability limit at $T = 650\ K, P = 1$ and 20 *atm*, and $\phi = 0.2$; (b) lean cool flames above the hot flame flammability limit at $\phi = 0.5$. The reduced kinetic model was from [29].

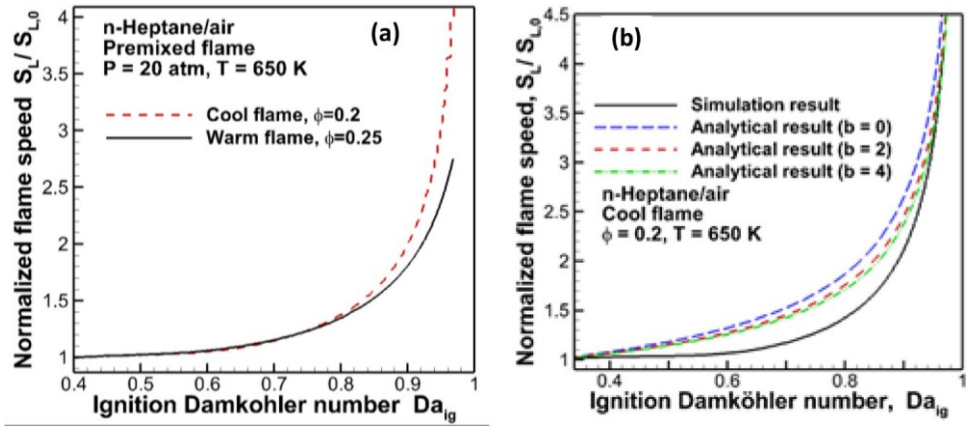

Fig. 40. Dependence of the normalized speed on the ignition Damköhler number. (a) comparison between cool flame and warm flame; (b) comparison between numerical modeling and analytical prediction in Eq.4 [91].

Figure 40a shows how the low temperature ignition Damköhler number affects the cool and warm flame speed. It is seen that both lean cool flame and warm flame speeds increase exponentially with the ignition Damköhler number. Note that when $Da_{ig,L}$ is below 0.8, the cool flame and warm flame have a similar trend. This is because at this condition, both cool flame and warm flame propagation depends on the speed of the leading cool flame front. However, with a further increase of $Da_{ig,L}$, the warm flame speed increases more slowly than the cool flame due to the higher activation energy of the HO_2 chemistry of ITI than that of LTI. This rapid flame speed increases with ignition Damköhler number suggests that the auto-ignition assisted cool flame and warm regimes need to be appropriately considered in compression ignition engines, knock, and flame lean-blow off in a flow recirculation zone. By using a three-zone flame structure: autoignition, convection-diffusion, and reaction zones with an one-step global reaction model, the laminar flame speed at a large ignition Damköhler number can be given as [91],

$$T_p = T_a / ln\left[\left(1 - Da_{ig}\right) e^{T_a/T_0} + Da_{ig} e^{T_a/T_f}\right] \quad (4a)$$

$$S_L \sim S_{L,Da_{ig}=0} \sqrt{\frac{T_f - T_0}{T_f - T_p}} \quad (4b)$$

where T_p is the temperature after the first-stage auto-ignition at Da_{ig}, T_a and T_f the reduced activation energy and flame temperature, and $S_{L,Daig=0}$ the laminar flame speed at $Da_{ig} = 0$. It is seen in Fig. 40b that the analytic expression can capture well the trend of the flame speed dependence on ignition Damköhler number, but deviates quantitatively from the computational result with the detailed kinetic model. The results of the auto-ignition assisted flame propagation in

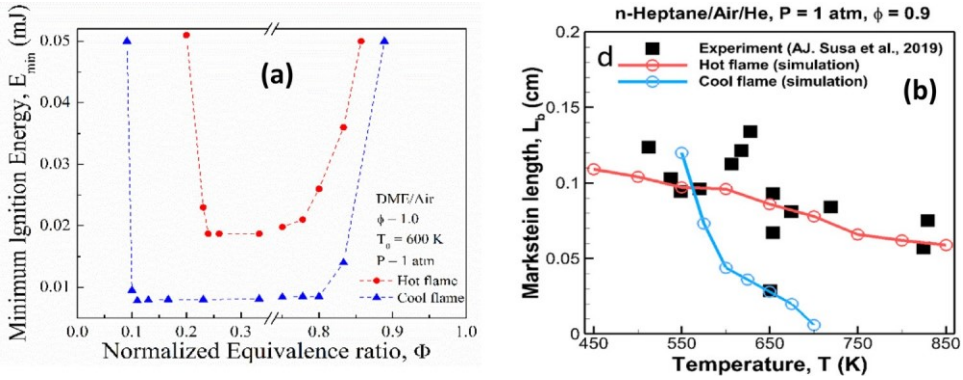

Fig. 41. (a) Comparison of the predicted minimum ignition energy of cool flame and hot flame for DME/air mixtures[108], (b) Comparison of measured and computed cool flame and hot flame Markstein length of n-heptane/air/He mixtures [106], the kinetic model was from [29].

Figs. 39 and 40 provide good understanding of the dynamics of low temperature flames under engine conditions.

4.2. The minimum ignition energy of cool flames and the effect of flame stretch

If the cool flame burning is important, one would ask: (1) how to initiate a propagating cool flame? (2) What is the cool flame minimum ignition energy [105,108,200,201]? And (3) how does the flame stretch affect the flame propagation. Ju et al. [29] and Zhang et al. [105] simulated the unsteady cool flame initiation by a hot spot. Recently, Zhang et al. [106] and Yang et al. [108] simulated the stretch effect on unsteady spherical flame propagation. Figure 41a shows the computed minimum ignition energy of DME/air mixtures by using the critical ignition radius [200,202] in an outwardly propagating spherical flame. It is seen that not only the cool flame has a broader flammable region on both fuel lean and rich sides but also has much lower ignition energies than that of the hot flames. Figure 41b show the comparison of computed [106] and measured [99] Markstein length of cool flames and hot flames of an n-heptane/air/He mixture at different mixture temperatures. It is seen that at high mixture temperatures, the cool flame Markstein length is much smaller than that of hot flame. However, at lower initial temperature, both of them become very close. Therefore, the studies of cool flame open a new research direction in laminar flames. One should question the applicability of the hot flame theories and models in cool flames.

4.3. Observation of cool flames and double flames in shock tube experiments

To measure flame speeds at elevated temperature and pressure, Hanson and co-workers [99,106] conducted experimental studies of outwardly propagating flames using a shock tube. Figure 42a shows the flame kernel images of an *n*-C_7H_{16}/O_2/Ar/He mixture at 732 K and 191.5 KPa, respectively, with laser ignition timing before and after the 1st-stage auto-ignition. It is interesting to note that if the laser ignition timing is earlier than the LTI, there was a double-flame structure. However, if the ignition timing is after the LTI, only one flame front exists. Although the mechanism of the double-flame structure captured with OH* chemi-luminescence was not clear, it is evident that the outcome is affected by the LTI. Figure 42b shows the comparison between the measured flame speeds and the prediction by high temperature chemistry. It is seen that the non-linear flame speed dependence on mixture temperature was not captured by the high temperature kinetic model.

To understanding this puzzling observation and the nonlinear flame speed dependence on temperature, Zhang et al. [106] compared the computed and measured flame speed evolution of an outwardly propagating spherical flame as a function of auto-ignition Damköhler number after the hot spot ignition. The modeling results in Fig. 43a show that after the hot spot ignition, there are five different burning regimes, I: a hot spot driven flame kernel, II: a double flame, III: a transient flame transition from a double flame to a hot flame, IV: hot flame, and V: auto-ignition. Figure 43b shows the experimentally measured flame front trajectory and flame speed using OH*. It is seen that the flame regimes are captured very well by the modeling. However, due to the uncertainty in cool flame chemistry, the modeling prediction could not capture the same flame trajectory at the same composition conditions.

Nevertheless, by including the LTC and ITC, the predicted flame speeds via the unsteady transition from a warm flame to a hot flame in Fig. 43 agree well with the measured nonlinear flame speed dependence on temperature in 42b.

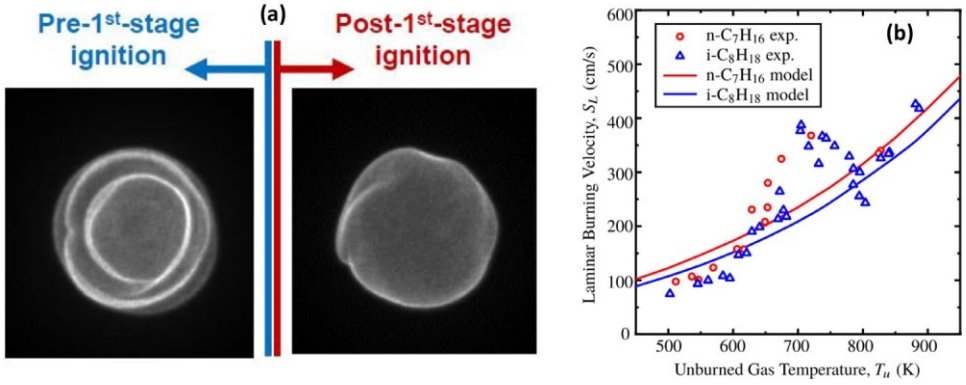

Fig. 42. (a) Images of flame kernel of an n-$C_7H_{16}/O_2/Ar/He$ mixture at $\phi = 0.9$, $T = 732$ K and $P = 91.5$ kPa laser ignition timing before and after the 1st-stage auto-ignition. (b) The measured and predicted laminar flame speeds as a function of unburned gas temperature for n-heptane and isooctane mixtures[99]. The kinetic model was from [29].

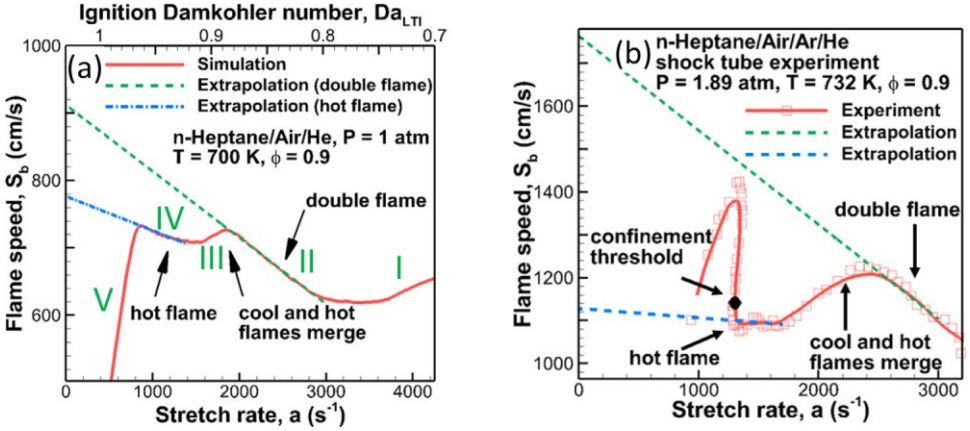

Fig. 43. (a) Numerical results for the relation between the flame speed and stretch rate for hot spot ignited spherically propagating double flame and hot flame at $P = 1$ atm, $T = 700$ K, φ=0.9 using n-Heptane/Air/He mixtures; (b): experimental results for the relation between the flame speed and stretch rate for double flame and hot flame at $P = 1.89$ atm, $T = 732$ K, φ=0.9 using n-Heptane/Air/Ar/He mixtures [106]. The kinetic model was from [29].

5. Impact of cool flames and warm flames on turbulent combustion

5.1. Comparison of flame length scales with turbulent length scales

Figure 44a shows a schematic comparison of different flame length scales and turbulent length scales. It is seen that for hot flame flames, the reaction zone thickness (δ_r) in near stoichiometric conditions are thinner than the Kolmogrov scale (η) of turbulence. Moreover, the rapid temperature rise in the reaction zone significantly increases the flow viscosity and quickly dissipates the microscale vortex in the Kolmogrov scale. Therefore, the turbulence-chemistry interaction for hot flame often occurs only in the preheating zone in a flame length scale (δ_f), even at a very high turbulent Reynolds number [203]. However, for cool flames, the reaction zone thickness ($\delta_{r,C}$ in Fig. 44) can be thicker than the Kolmogrov scale because of its lower flame speed. In addition, the temperature rise in a cool flame is very modest so that the increase of viscosity is small. Therefore, there can be strong turbulence chemistry interaction for cool flame flames. For the warm flame, as also shown in Fig. 44b, the separation distance between the leading cool flame and the trailing intermediate temperature flame front can vary from submillimeter to centimeters. As such, turbulence will have a stronger impact on the warm flame structure and results in unsteady transitions between cool flame, warm flame, and hot flame. However, only few turbulent combustion studies have been carried out for turbulent cool flames and warm flames [88,124,204,205], especially at elevated temperature and pressure.

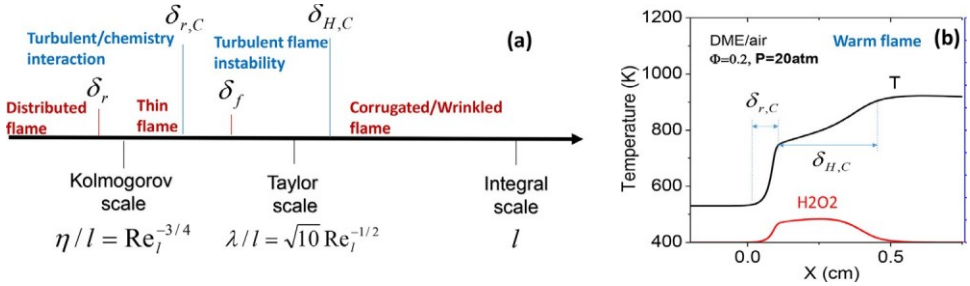

Fig. 44. (a) Comparison of flame length scales with turbulent length scales. (b) Structure of a high pressure DME/air warm flame [168].

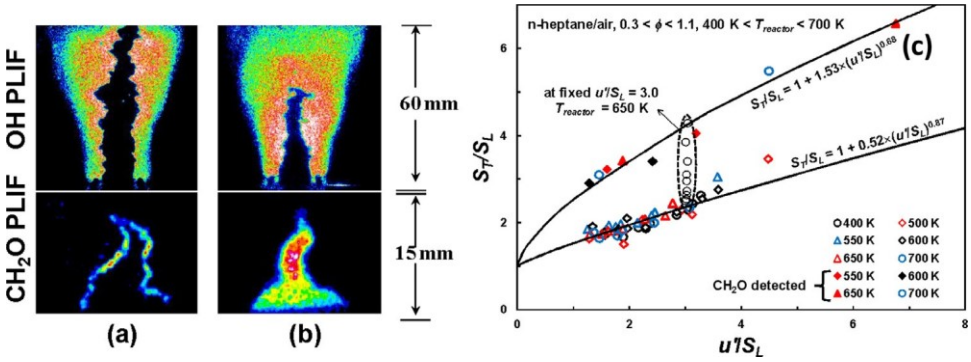

Fig. 45. OH and CH_2O PLIF images for turbulent premixed flames in (a) the chemically-frozen regime at 500 K and (b) the LTI regime at 650 K. Both sets of images are at ϕ=0.5 with a reactor flow residence time of 100 ms. (c): Measured turbulent burning velocity normalized by laminar burning velocity, S_T/S_L as a function of turbulent intensity, u'/S_L at (a) low LTI Damköhler numbers and (b) high LTI Damköhler numbers. Solid symbols represent the cases where CH_2O was detected at the nozzle exit. Black circles are from the measurements with constant u'/S_L [206].

5.2. *Experimental studies of turbulent cool flames*

To understand LTC auto-ignition assisted turbulent flame propagation, Won et al. [206,207] developed a Reactor-Assisted Turbulent Slot (RATS) burner to study how LTI affected premixed turbulent flame speed, flame structure, and flame regime. Won et al. [206] measured the dependence of OH and CH_2O PLIFs and the normalized turbulent flame speed (S_T/S_L) of n-heptane turbulent flames on turbulence intensity and LTI using a RATS burner (Fig. 45). With the increase of reactor temperature and the progress of LTI, Figure 45a and 45b shows that the OH and CH_2O distributions had significant changes. At 500 K, only a small layer of CH_2O was present in the preheat zone of the hot flame front (front of OH PLIF). Therefore, the pre-flame mixture was still in the classical chemically-frozen regime ($Da_{ig,C} \to 0$). However, when the initial mixture temperature was increased to 650 K, Figure 45b shows that a significant amount of CH_2O was formed upstream of the hot flame front via LTC, indicating that the turbulent pre-flame mixture was in the LTI regime ($Da_{ig,C} > 0$). As a result, the turbulent burning velocity shown in Fig. 45c was also found to have two different flame regimes: (a) a chemically-frozen regime at 500 K and (b) a LTI regime at 650 K. The turbulent flame speeds in the LTI regime were much higher than that in the chemically-frozen regime. The increase of turbulent flame speed in the LTI regime was caused by the change of the reactivity and transport properties of the partially burning pre-flame mixture. Moreover, the results showed that the turbulent flame speed could be continuously increased by raising the LTI Damköhler number (dotted circles in Fig. 45c for $Da_{ig,C} \to 1$), suggesting that similar to the auto-ignition assisted laminar flame speed in Fig. 40, the turbulent burning velocity for fuels with LTC is not uniquely defined and strongly depends on $Da_{ig,C}$. To investigate the impact of LTC on turbulent flame propagation, Windom et al. [207] performed a Damköhler scaling analysis, which indicated that the increase in turbulent flame speed in the LTI regime was indeed originated from an increase in laminar flame speed, a decrease in Lewis number, and an increase in turbulence intensity due to the changes in mixture composition and temperature from LTI.

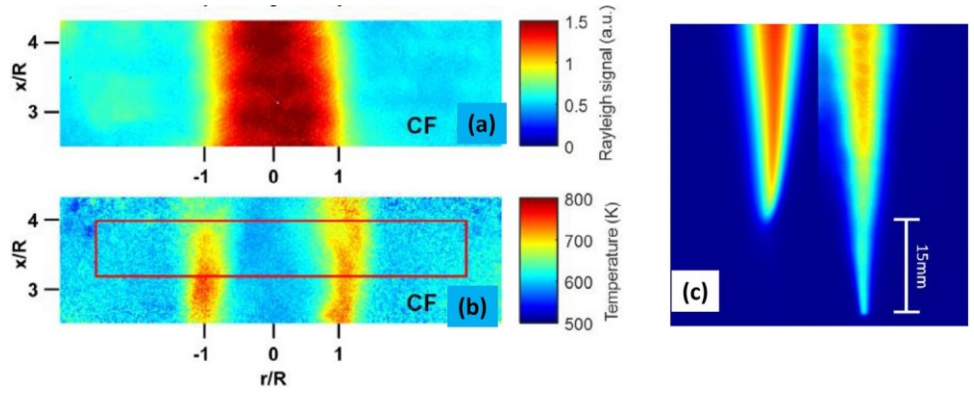

Fig. 46. (a) Rayleigh scattering signal for a cool flame, (b) temperature for a cool flame. The red box indicates where the time-averaged statistics will be computed, and (c) DNS (left) and experimental CH_2O PLIF, (right) profiles of mean CH_2O slightly above the nozzle [103]. The kinetic model was from [177].

More recently, a Co-flow Axisymmetric Reactor Assisted Turbulent (CARAT) burner was developed for the investigation of turbulent non-premixed DME cool flames for direct comparison to computational studies [103]. Two-dimensional mixture fraction and temperature measurements were derived from the acetone PLIF and Rayleigh scattering signals (Fig. 46a), respectively. A DNS database of an isolated turbulent non-premixed cool flame based on the experimental CARAT burner was created. The results showed that the global flame structure was found to be dependent on the inlet boundary conditions, such that a 10 K difference in flow temperature switched the flame from being lifted to anchored at the burner (Fig. 46b). Comparisons of the DNS to experimental measurements found good agreement for temperature and mixture fraction profiles in physical space with the adjusted boundary condition. Examination of a differential diffusion parameter in the DNS found that an effective Lewis number of unity was valid for this configuration, even though the Reynolds number is considerably lower than typical values that support unity effective Lewis numbers in hot flames. This was attributed to the very low change in temperature, viscosity, and therefore Reynolds number across a cool flame compared to a hot flame. This study was further extend to auto-ignition assisted turbulent non-premixed flames [104,207]. The results showed that the flame lift-off height was strongly dependent on the ignition delay of LTC. This result gave good explanation to the occurrence of LTI assisted turbulent flame flashback.

5.3. *Computational studies of turbulent cool flames*

Many turbulent cool flame simulations have been conducted and these studies provided insights of low temperature turbulent combustion at engine conditions. Krisman et al. [121] simulated laminar DME flames in a nonpremixed mixing layer at 40 atm over a range of oxidizer temperatures and inlet velocities. The results showed a gradual transition from a flame stabilized by thermal and molecular diffusion to a flame stabilized by autoignition with increasing temperature. At 700 K, the flame had a classical tribrachial structure. At a higher temperature under an auto-ignition condition (900 K), it was found that the flame consisted of a main tribrachial structure and an additional upstream branch due to LTI, and was therefore termed as a tetrabrachial flame. At 1100 K and 1300 K, two upstream branches were observed in addition to the main tribrachial structure, one due to LTI and the other due to HTI. These flames were thus termed pentabrachial flames. Deng et al. [94] also conducted DNS modeling of DME/air non-premixed coflow flames at air temperatures between 700-1100 K. A multi-brachial flame structure was observed near 800 K. Therefore, LTI and cool flames can significantly modify flame modes and change the classical understanding of non-premixed flames. Bansal et al. [208] conducted both two- and three-dimensional DNS studies of auto-ignition phenomena in stratified DME/air turbulent mixtures. In this study, the contributions of homogeneous auto-ignition, spontaneous ignition front propagation, and premixed deflagration towards the total heat release were quantified.

Krisman et al. [197,209] and Borghesi et al. [123] further extended low-temperature non-premixed combustion modeling to a 2-D and 3-D turbulent mixing layer for DME and n-dodecane at diesel engine-relevant conditions. Figure 47a shows an image of a turbulent n-dodecane planar temporal jet undergoing low-temperature ignition at 25 bar (H_2O_2 mass fraction). The broad H_2O_2 mole fraction distribution indicates the existence of strong low temperature combustion at engine

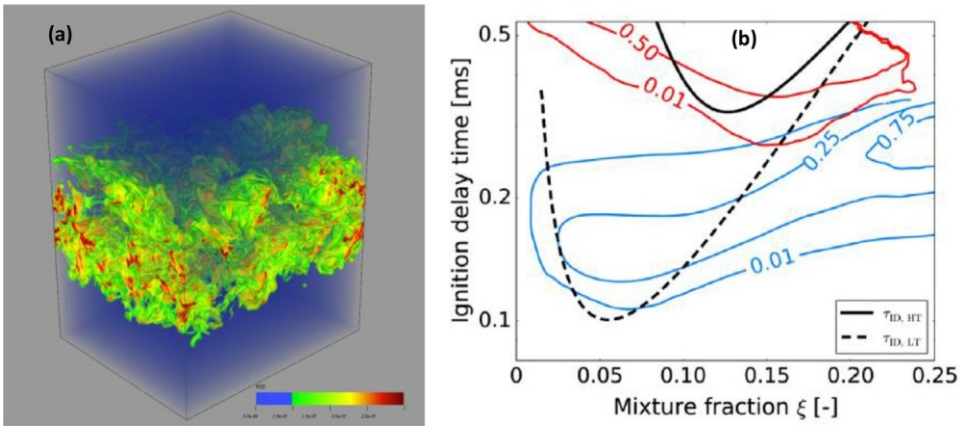

Fig. 47. (a) The temporal jet configuration investigated in the DNS study, highlighting the streamwise (x), spanwise (z) and inhomogeneous (y) directions of the flow[123]. The image shows the volumetric rendering of H_2O_2 mass fraction, Y_{H2O2}, at $t = 0$. 5 ms. The green color corresponds to $Y_{H2O2}=10^{-3}$, and the red color to $Y_{H2O2}=3\times10^{-3}$. (b) Blue lines: fraction of fluid elements that have undergone LTI. Red lines: fraction of fluid elements that have undergone HTI. Black lines: homogeneous ignition delay times for LTI (dashed line) and HTI (solid line).

related conditions. Figure 47b shows that cool flame propagation and turbulent diffusion result in faster low-temperature ignition on the fuel rich side which accelerates high-temperature ignition, resulting in overall shorter ignition delays and ignition occurring at richer conditions than the preferred mixture fraction based on homogeneous ignition. These results were also observed by Krisman et al. [197,209] for diluted di-methyl ether flames and are consistent with experiments by Scott Skeen and Lyle Pickett in diesel engines [34,210,211].

6. Cool flames and warm flames as platforms for fuel chemistry model validation

Despite extensive studies of LTC and ITC [59,60,141,142,152], there still exist large uncertainties in the reaction rates and pathways even for extensively studied fuels such as DME and *n*-heptane [86,95,97,177,185,212–214], due to the difficulty in quantitative measurements of HO_2, QOOH, RO_2, and O_2QOOH radicals as well as large intermediate isomers at low and intermediate temperatures, whose reactions with OH and HO_2 contribute significantly to the low temperature heat release rate. Cool flames and warm flames provide a new platform to validate LTC and ITC kinetic models involving strong chemistry and combustion heat release coupling [83,84,86,87,95,215]. For a homogeneous mixture, shock tube, rapid compression machine, flow reactor, and jet-stirred reactor experiments [11,128,129,216–219] have successfully been used to develop and validate kinetic models using ignition delay time and species profile (Fig. 48a). On the other hand, flame extinction limits and laminar flame speeds have been used to constrain the heat release rate and diffusive transport coupling for HTC (Fig. 48b). Accurate description of the heat release rate in LTC and ITC under engine conditions requires validation of coupled chemico-physical and transport processes in combustion. However, for LTC and ITC, until very recently, there have been no such experiment data available to validate the heat release rate and transport coupling for full-strength mixtures. The cool flames, warm flames, and double flames [99,106] provide new platforms for fuel chemistry model and transport model validation (Fig. 48b).

To illustrate the challenges in LTC and ITC kinetic model validation for accurate prediction of low temperature heat release rate, Figure 49a [86] shows the comparison of the predicted and measured non-premixed flame extinction limits for large *n*-alkanes in a counterflow burner. Reduced models were created from the Lawrence Livermore National Laboratory detailed model [220] through a path flux analysis method [221]. Significant model discrepancies for LTC are illustrated in Fig. 49a. First, the measured hot flame extinction (HFE) limits of the different *n*-alkanes agree well with the model predictions. However, although the predicted and measured cool flame extinction (CFE) limits both show strong dependence on the length of the carbon chain, the predicted CFEs are much higher than that of experiments. The LTC sensitivity on carbon chain length is consistent with previous experiments [173,222–230], but the large difference in CFEs between model prediction and experiments is inconsistent with the good prediction of ignition delay time of large *n*-alkanes [137,220] and could not be solely explained by the uncertainty in transport coefficients.

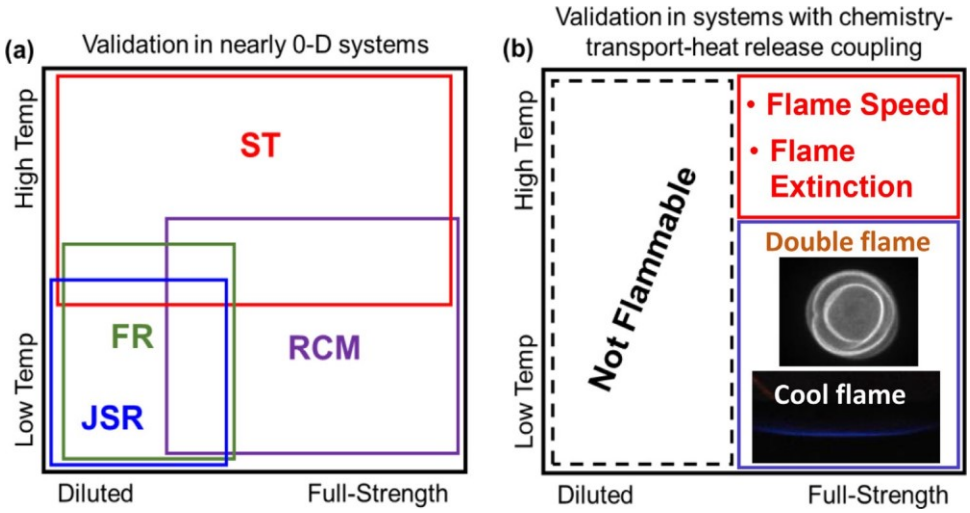

Fig. 48. Experiment apparatus to validate chemical kinetic models as a function of fuel dilution and temperature: (a) nearly homogeneous experiments and (b) Experiments with chemistry and transport coupling. ST: shock tube; RCM: rapid compression machine; FR: flow reactor; JSR: jet-stirred reactor.

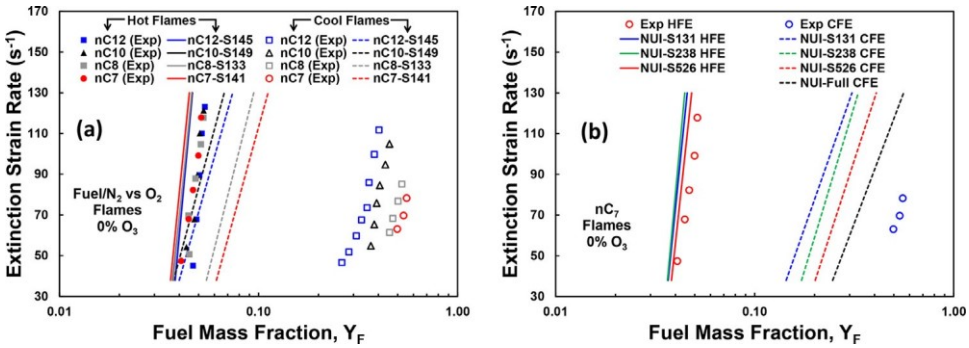

Fig. 49. (a) Comparison between the experimentally measured and numerically predicted extinction limits for *n*-alkane flames. (b) Effect of model reduction on the numerically predicted extinction limits for *n*-heptane flames (See detailed description of the reduced kinetic models in [86]).

Therefore, this large discrepancy can be inferred that the cool flame heat release rate and its coupling with diffusive transport for the CFE limit are not well constrained in current low-temperature kinetic models. To prove this thinking, Figure 49b [86] shows the comparison between the measured and predicted *n*-heptane HFE and CFE limits using both the detailed model from NUI-Galway [231] and different reduced models with 131, 238, and 526 species, respectively. It is seen that the HFE limits for *n*-heptane were well predicted and shown to be nearly insensitive to the reduced model size. On the other hand, the *n*-heptane cool flames displayed a consistent increase in reactivity as the model size decreases. Similar large discrepancy was also observed in DME cool flames [134,232]. A further comparison between the difference in the elementary reactions for LTC and HTC of n-heptane mixtures shows that for LTC, the key heat production reactions rely primarily on reactions involving large, fuel molecule-sized (C_7) molecules and intermediate species. However, the major heat release rate reactions for HTC are those involving only C_0–C_2 species [173]. Since the C_7 chemistry in the *n*-heptane model has large uncertainties in reaction rate constants and thermochemistry for important species at LTC, this explains why the experiments agreed well with predictions for the HFE limits but poorly for the CFE limits. Therefore, the cool flames, warm flames, and double flames in counterflow and shock tube experiments provide excellent platforms to constrain the heat release rates in LTC and ITC (Fig. 48b).

To demonstrate the usefulness of the cool flame platform in model validation and development, a more comprehensive assessment of DME/CH_4

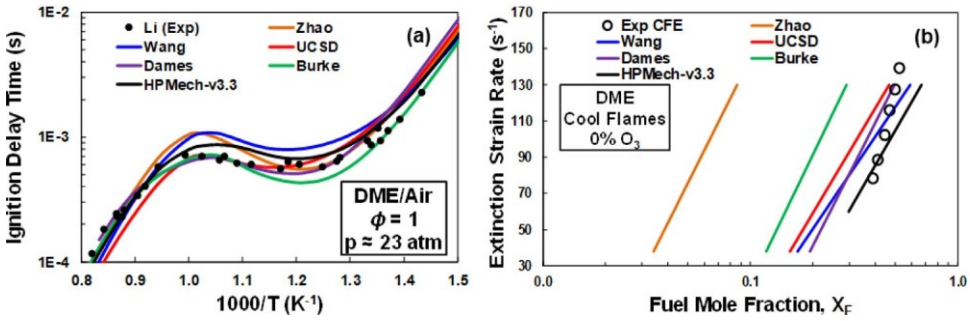

Fig. 50. Literature model comparisons to experimental data for DME (a) ignition delay times [234] and (b) CFE limits (see details for kinetic models in [215]).

chemical kinetic models was re-examined by Reuter et al. [215]. Comparisons between the models by Wang et al. [177], Dames et al. [213], Zhao et al. [145], UCSD [233], Burke et al. [212], and HP-Mech/DME [215] for non-premixed CFE limits and ignition delay times are shown in Fig. 50 [215]. It is seen in Fig. 50a that all of these models predicted reasonably well the experimental ignition delay times [234] at low and intermediate temperature. However, a large disparity between the models for the non-premixed CFE limits is seen in Fig. 50b. Models by Wang et al., Dames et al., and HP-Mech/DME updated with the cool flame validation targets improved the predictions of both ignition and cool flames.

7. Future research for cool flames and warm flames

Since 2010, significant progress has been made in experimental observation and computational modeling of non-premixed and fuel lean cool flames, warm flames, double flames, and three-stage flames by different research groups. These studies have presented us a clearer picture and understanding of the overall dynamics, chemistry, and burning limits of low temperature flames. However, there are still large discrepancies between model prediction and experiment of cool flames. Few cool flame and warm flame experimental data are available for high pressure, spray, and turbulent combustion, especially involving real fuels and low carbon alternative fuels under engine conditions. The transition between low temperature ignition, cool flame, warm flame, double flame, and hot flame are not well-understood for auto-igniting mixtures relevant to engine conditions. The minimum ignition energy and the effect of transport on cool flames, warm flames, and transient double flames are not well explored. In addition, the role of low temperature combustion in engine knock, deflagration to detonation transition (DDT), lean blow-off, and flame stabilization in a recirculation zone have not been well-understood.

7.1. High pressure cool flames and warm flames under auto-ignition conditions

Advanced engines run up to 100 atm. However, cool flame experiments using micro-reactor, counterflow flames, droplets, and shock tube were mostly done under or close to atmospheric pressure. No measured cool flame speeds are currently available even at atmospheric conditions. No premixed warm flames have been observed on fuel lean conditions. As discussed above, cool flames and warm flames can serve as new platforms for understanding low temperature combustion and kinetic model validation. It is necessary to extend the cool flame and warm flame experiments to higher pressure and elevated temperature. Shock tube experiments provide a new opportunity to measure cool flame and double flame speeds at elevated pressure and to observe unsteady transition between different flame regimes under auto-igniting conditions if the experimental data can be appropriately interpreted. However, flame instability and diagnostics of cool flame and double flame in shock tube can be a challenging issue. Moreover, the dynamics of cool flames such as the minimum ignition energy and the stretch effects on cool flame propagation has not been experimentally addressed, although several numerical simulations have shown that the minimum ignition energy and Markstein length of cook flames are different from that of hot flames. Cool flame and warm flame studies open a new research frontier in laminar flames and low temperature combustion.

7.2. Low temperature and high pressure kinetic model development for low carbon fuels

The current kinetic models which can well-reproduce low temperature and high temperature ignition delays may fail to predict extinction limits and flame speeds of cool flames and warm flames. One of the main reasons is the lack of validation targets of cool flames and warm flames. Therefore, in the future model validations, the cool flame,

warm flame, and double flame data should be obtained and used as additional model validation targets to constrain the heat release rates at LTC and ITC. Another reason is the large uncertainty of LTC and HO_2 chemistry in ITC. For low temperature chemistry, the key challenges are to quantify key intermediate radicals and intermediate species such as QOOH, ketohydroperoxide, alkyl peroxy radicals, HO_2, and partially oxidized large isomers [152]. Although several advances have been made in quantifying these key species [185,235–240], these methods need to be extended to high pressure experiments. To address kinetics at high pressure engine conditions, low temperature experiments up to 100 atm are necessary. Moreover, at high pressure, the real gas effects, non-equilibrium kinetics, and the termolecular reactions may also need to be explored [241–243]. Recently, new high pressure experimental facilities at and above 100 atm have been developed recently [157,244]. Furthermore, recent progress in accurate electronic structure calculations with appropriate consideration of multi-reference configuration interaction has made it possible to theoretically compute the rates of these reactions [156,157,245–247]. As such, by combing the uncertainty quantification and sensitivity analysis methods [248] using the experimental data of low temperature ignition and cool flames to identify the key elementary reactions and the uncertainty in their rates, the predictability of LTC and ITC models can be improved. In addition, recent progress in data science based analysis [249,250] may also help to design the critical experiments and extract more accurate rate constants systematically.

7.3. Cool flames in spray combustion and turbulent combustion

Most engines involve spray combustion. Spray vaporization is complicated by multi-component vaporization and gradient distributions of temperature, fuel concentration and compositions. Although recent microgravity studies provide good understanding of single droplet cool flames, droplet-cool flame interaction, droplet-droplet interaction, and group low temperature combustion have not been emphasized. Moreover, low temperature ignition and its transition to cool flames and warm flames and hot flames in spray combustion are not well understood. Computational modeling of low temperature spray combustion is also scarce. Numerical modeling of low temperature spray combustion at engine conditions are needed to understand the critical low temperature flame dynamics in engine applications.

7.4. Control and chemical sensitization of low temperature combustion

To control engine heat release rate and engine ignition timing, as shown by the research of RCCI engines [7], chemical sensitization of low temperature combustion and cool flames is an effective way because their sensitivities to low temperature radical production and quenching. Plasma, ozone, NO_x, and diesel additives all create different reaction pathways in changing low temperature combustion in different temperature ranges. Quantitative studies of these chemical sensitizers on cool flames and warm flames as well as low temperature combustion kinetics are needed to develop an active control method for low temperature combustion and advanced engines. In addition, a recent study shows that low temperature combustion kinetics can also affect plasma properties and instability [251]. As such, it is necessary to understand plasma-combustion chemistry interaction for lean burn engine ignition.

7.5. Impact of low temperature combustion on advanced engines

Cool flames have been thought to affect engine knock. There have been extensive studies of LTC effect on engine knock [32,252–256]. However, the detailed mechanism of the impact cool flame on engine knock has not been well-understood. In particular, the effects of LTC and turbulence-chemistry coupling on ignition kernel development and its transition to detonation is not well explored. Recently, several experimental studies showed that ozone addition in premixed ethylene and hydrogen mixtures can accelerate ignition to detonation transition in a mesoscale channel [257,258]. However, the role of low temperature and intermediate temperature chemistry on deflagration to detonation transition has not been well examined. Moreover, although experimental data have shown that flame stabilization, lean blow-off, and flashback are affected by low temperature auto-ignition, the effect of auto-ignition assisted low temperature flames on flame stabilization is not well studied. Therefore, in future studies, the impacts of low temperature auto-ignition assisted flame propagation on engine knock, deflagration to detonation transition, lean blow-off, and flame flashback need to be addressed.

Declaration of Competing Interest

None.

Acknowledgment

The work presented here is a collaborative outcome of many research groups. YJ would like to thank particularly Jacqueline H. Chen, Zheng Chen, Daniel L. Dietrich, Frederick L. Dryer, Tanvir Farouk, Ronald Hanson, Chung K. Law, Kaoru Maruta, Michael E Mueller, Vedha Nayagam, Christopher Reuter, Forman A. Williams, Sang

Hee Won, Omar Yehia, Tianhan Zhang, and Peng Zhao for sharing their results, collaborations, and encouraging discussions. He also would like to thank all his graduate students, postdocs, and the grant support from NSF CBET 1903362, ARO W911NF-19-2-0127,NASA NNX16AK07G, and DOE DE-SC0001198, DE-**SC0021135** and DE-SC0020233.

References

[1] Summary for Policymakers of IPCC Special Report on Global Warming of 1.5°C. http://www.ipcc.ch/news_and_events/pr_181008_P48_spm.shtml, 2018.
[2] N. Iida, in: Proceedings of the Public Symposium on Innovative Combustion Technology, 2019.1.28., 2019.
[3] S. Kimura, in: Proceedings of the KAUST Research Conference: New Combustion Concept, March 6-8, 2017, 2017.
[4] J.E. Dec, *Proc. Combust. Inst.* 32 (2009) 2727–2742.
[5] D. Splitter, R. Reitz, R Hanson, *SAE Int. J. Fuels Lubr.* 3 (2010) 742–756.
[6] G.A. Lechner, T.J. Jacobs, C.A. Chryssakis, D.N. Assanis, R.M Siewert, *SAE Tech. Pap.* (2005).
[7] D. Splitter, M. Wissink, D. DelVescovo, R.D Reitz, *SAE Tech. Pap.* (2013).
[8] K. Kohse-Höinghaus, P. Oßwald, T.A. Cool, et al., *Angew. Chem. Int. Ed.* 49 (2010) 3572–3597.
[9] J. Farrell, *Co-Optimization of Fuels & Engines (Co-Optima) Initiative: Recent Progress on Light–Duty Boosted Spark-Ignition Fuels/Engines*, National Renewable Energy Laboratory (NREL), Golden, COUnited States, 2017.
[10] M. Colket, J. Heyne, M. Rumizen, et al., *AIAA J.* 55 (2017) 1087–1104.
[11] W.J. Pitz, C.J. Mueller, *Prog. Energy Combust. Sci.* 37 (2011) 330–350.
[12] A.K. Agarwal, *Prog. Energy Combust. Sci.* 33 (2007) 233–271.
[13] M. Zheng, T. Li, X Han, *Fuel* 142 (2015) 28–37.
[14] M.P. Musculus, P.C. Miles, L.M Pickett, *Prog. Energy Combust. Sci.* 39 (2013) 246–283.
[15] T. Lachaux, M.P Musculus, *Proc. Combust. Inst.* 31 (2007) 2921–2929.
[16] J.S. Heyne, E. Peiffer, M.B. Colket, et al., in: Proceedings of the AIAA Aerospace Sciences Meeting, 2018, p. 1667.
[17] H. Davy, *Philos. Trans. R. Soc. Lond.* 107 (1817) 77–85.
[18] W. Perkin, *J. Chem. Soc. Trans.* 41 (1882) 363–367.
[19] P. Lignola, *Prog. Energy Combust. Sci.* 13 (1987) 75–96.
[20] J. Griffiths, S Scott, *Prog. Energy Combust. Sci.* 13 (1987) 161–197.
[21] J Griffiths, *Prog. Energy Combust. Sci.* 21 (1995) 25–107.
[22] D. Townend, E. Chamberlain, *Proc. R. Soc. Lond. Ser. A Math. Phys. Sci.* 154 (1936) 95–112.
[23] D. Townend, *Chem. Rev.* 21 (1937) 259–278.
[24] K. Williams, J. Johnson, H Carhart, in: Proceedings of the Symposium (International) on Combustion, Elsevier, 1958, pp. 392–398.
[25] F. Williams, R. Sheinson, *Combust. Sci. Technol.* 7 (1973) 85–92.
[26] F. Williams, D. Indritz, R Sheinson, *Combust. Sci. Technol.* 11 (1975) 67–73.
[27] Y. Ju, C.B. Reuter, O.R. Yehia, T.I. Farouk, S.H Won, *Prog. Energy Combust. Sci.* 75 (2019) 39.
[28] J.P. Szybist, S.W. Wagnon, D. Splitter, W.J. Pitz, M Mehl, *SAE Int. J. Engines* 10 (2017) 2305–2318.
[29] Y. Ju, W. Sun, M.P. Burke, X. Gou, Z Chen, *Proc. Combust. Inst.* 33 (2011) 1245–1251.
[30] L. Manofsky, J. Vavra, D.N. Assanis, A Babajimopoulos, *SAE Tech. Pap.* (2011).
[31] X. Lu, D. Han, Z Huang, *Prog. Energy Combust. Sci.* 37 (2011) 741–783.
[32] G. Kalghatgi, *Proc. Combust. Inst.* 35 (2015) 101–115.
[33] L. Hildingsson, G. Kalghatgi, N. Tait, B. Johansson, A Harrison, *SAE Tech. Pap.* (2009).
[34] S.A. Skeen, J. Manin, L.M Pickett, *Proc. Combust. Inst.* 35 (2015) 3167–3174.
[35] M. Colket, S. Zeppieri, Z. Dai, D Hautman, in: Proceedings of the 5th Annual Fuel Research Meeting Multi-Agency Coordinating Council for Combustion Research, Livermore, CA, Sandia National Laboratories, 2012.
[36] Emeléus H.J. J. Chem. Soc. (Resumed). 1929:1733–9.
[37] Hsieh M., Townend D. J. Chem. Soc. (Resumed). 1939:337–40.
[38] J. Topps, D. Townend, *Trans. Faraday Soc.* 42 (1946) 345–351.
[39] H.C. Bailey, R. Norrish, in: Proceedings of the Royal Society of London A: Mathematical, Physical and Engineering Sciences, The Royal Society, 1952, pp. 311–330.
[40] W. Agnew, J. Agnew, K Wark Jr, in: Proceedings of the Symposium (International) on Combustion, Elsevier, 1955, pp. 766–778.
[41] R.J. Foresti, in: Proceedings of the Symposium (International) on Combustion, Elsevier, 1955, pp. 582–589.
[42] A. Fish, I.A. Read, W.S. Affleck, W.W Haskell, *Combust. Flame* 13 (1969) 39–49.
[43] P. Ballinger, P. Ryason, in: Proceedings of the Symposium (International) on Combustion, Elsevier, 1971, pp. 271–277.
[44] B. Gray, *Trans. Faraday Soc.* 65 (1969) 1603–1613.
[45] P. Barat, C. Cullis, R Pollard, in: Proceedings of the Royal Society London A, The Royal Society, 1971, pp. 469–492.
[46] J.F. Griffiths, T. Inomata, *J. Chem. Soc. Faraday Trans.* 88 (1992) 3153–3158.
[47] W.G. Agnew, J.T. Agnew, *Ind. Eng. Chem.* 48 (1956) 2224–2231.
[48] C.K. Law, G.M. Faeth, *Prog. Energy Combust. Sci.* 20 (1994) 65–113.
[49] M. Kono, K. Ito, T. Niioka, T. Kadota, Sato Ji, in: Proceedings of the Symposium (International) on Combustion, Elsevier, 1996, pp. 1189–1199.
[50] K. Maruta, M. Yoshida, H. Guo, Y. Ju, T Niioka, *Combust. Flame* 112 (1998) 181–187.
[51] V. Nayagam, J. Haggard, R. Colantonio, et al., *AIAA J.* 36 (1998) 1369–1378.
[52] P.D Ronney, in: Proceedings of the Symposium (International) on Combustion, Elsevier, 1998, pp. 2485–2506.
[53] V. Nayagam, J.B. Haggar, F.L. Dryer, F.A Williams, in: Proceedings of the Conference and Exhibit on International Space Station Utilization, Cape Canaveral, FL, 2001, p. 5044.

[54] V. Nayagam, J. Haggard Jr, R. Colantonio, et al., *AIAA J.* 36 (1998) 1369–1378.
[55] M. Foster, H. Pearlman, *Combust. Flame* 147 (2006) 108–117.
[56] H. Pearlman, *Combust. Flame* 121 (1999) 390–393.
[57] H. Pearlman, *Combust. Flame* 121 (2000) 390–393.
[58] H. Pearlman, *Combust. Flame* 148 (2007) 280–284.
[59] H.J. Curran, P. Gaffuri, W.J. Pitz, C.K Westbrook, *Combust. Flame* 114 (1998) 149–177.
[60] F. Battin-Leclerc, *Prog. Energy Combust. Sci.* 34 (2008) 440–498.
[61] C. Corre, F. Dryer, W. Pitz, C Westbrook, in: Proceedings of the Symposium (International) on Combustion, Elsevier, 1992, pp. 843–850.
[62] M. Tanabe, M. Kono, J. Sato, et al., *Combust. Sci. Technol.* 108 (1995) 103–119.
[63] A. Cuoci, M. Mehl, G. Buzzi-Ferraris, T. Faravelli, D. Manca, E Ranzi, *Combust. Flame* 143 (2005) 211–226.
[64] C.K. Law, P. Zhao, *Combust. Flame* 159 (2012) 1044–1054.
[65] H. Oshibe, H. Nakamura, T. Tezuka, S. Hasegawa, K Maruta, *Combust. Flame* 157 (2010) 1572–1580.
[66] A. Yamamoto, H. Oshibe, H. Nakamura, T. Tezuka, S. Hasegawa, K Maruta, *Proc. Combust. Inst.* 33 (2011) 3259–3266.
[67] M. Hori, A. Yamamoto, H. Nakamura, T. Tezuka, S. Hasegawa, K Maruta, *Combust. Flame* 159 (2012) 959–967.
[68] S. Suzuki, M. Hori, H. Nakamura, T. Tezuka, S. Hasegawa, K Maruta, *Proc. Combust. Inst.* 34 (2013) 3411–3417.
[69] S. Kikui, T. Kamada, H. Nakamura, T. Tezuka, S. Hasegawa, K Maruta, *Proc. Combust. Inst.* 35 (2015) 3405–3412.
[70] T.I. Farouk, F.L. Dryer, *Combust. Flame* 161 (2014) 565–581.
[71] T. Farouk, M. Hicks, F Dryer, *Proc. Combust. Inst.* 35 (2015) 1701–1708.
[72] T. Farouk, D. Dietrich, F. Alam, F Dryer, *Proc. Combust. Inst.* 36 (2017) 2523–2530.
[73] Tanvir Farouk, Daniel Dietrich, F.L Dryer, in: Proceedings of the Eastern States Section of the Combustion Institute, March 4-7, 2018, State College, Pennsylvania, 2018 State College, Pennsylvania.
[74] T. Farouk, D. Dietrich, F.L Dryer, *Proc. Combust. Inst.* 37 (2019) 3353–3361.
[75] D. Dietrich, R. Calabria, P. Massoli, V. Nayagam, F Williams, *Combust. Sci. Technol.* 189 (2017) 520–554.
[76] V. Nayagam, D.L. Dietrich, M.C. Hicks, F.A Williams, *Combust. Flame* 162 (2015) 2140–2147.
[77] V. Nayagam, D.L. Dietrich, F.A Williams, *AIAA J.* 54 (2016) 1235–1239.
[78] F.A. Williams, V. Nayagam, in: Proceedings of the AIAA Scitech 2019 Forum, 2019, p. 0729.
[79] V. Nayagam, D.L. Dietrich, P.V. Ferkul, M.C. Hicks, F.A Williams, *Combust. Flame* 159 (2012) 3583–3588.
[80] V. Nayagam, in: Proceedings of the 2nd Annual ISS Research and Development Conference, Denver, Colorado, 2013.
[81] D.L. Dietrich, V. Nayagam, M.C. Hicks, et al., *Microgravity Sci. Technol.* 26 (2014) 65–76.
[82] Won S.H., Jiang B., Diévart P., Ju Y., Sohn C.H. A new cool flame: establishment and studies of dynamics and kinetics. Proceedings of the 52nd Aerospace Sciences Meeting, (doi: 10.2514/6.2014-0818). AIAA paper-2014-08182014.
[83] S.H. Won, B. Jiang, P. Diévart, C.H. Sohn, Y Ju, *Proc. Combust. Inst.* 35 (2015) 881–888.
[84] C.B. Reuter, S.H. Won, Y Ju, *Combust. Flame* 166 (2016) 125–132.
[85] C.B. Reuter, S.H. Won, Y Ju, *Proc. Combust. Inst.* 36 (2017) 1513–1522.
[86] C.B. Reuter, M. Lee, S.H. Won, Y Ju, *Combust. Flame* 179 (2017) 23–32.
[87] A. Alfazazi, A. Al-Omier, A. Secco, H. Selim, Y. Ju, S.M Sarathy, *Combust. Flame* 191 (2018) 175–186.
[88] C.B. Reuter, O. Yehia, S.H. Won, et al., in: Proceedings of the AIAA Aerospace Sciences Meeting, 2018, p. 0678.
[89] C.B. Reuter, R. Zhang, O. Yehia, Y Ju, in: Proceedings of the AIAA Aerospace Sciences Meeting, 2018, p. 2184.
[90] M. Lee, Y. Fan, C.B. Reuter, Y. Ju, Y Suzuki, *Proc. Combust. Inst.* (2018) 37.
[91] T. Zhang, Y. Ju, in: Proceedings of the 11th U S National Combustion Meeting, Pasadena, California, 2019, pp. 1–4.
[92] S. Deng, P. Zhao, D. Zhu, C.K Law, *Combust. Flame* 161 (2014) 1993–1997.
[93] P. Zhao, W. Liang, S. Deng, C.K Law, *Fuel* (2015).
[94] S. Deng, P. Zhao, M.E. Mueller, C.K Law, *Combust. Flame* 162 (2015) 3437–3445.
[95] S. Deng, D. Han, C.K Law, *Combust. Flame* 176 (2017) 143–150.
[96] W. Sun, S.H. Won, Y Ju, *Combust. Flame* 161 (2014) 2054–2063.
[97] M. Hajilou, T. Ombrello, S.H. Won, E Belmont, *Combust. Flame* 176 (2017) 326–333.
[98] C.B. Reuter, V.R. Katta, O.R. Yehia, Y Ju, *Proc. Combust. Inst.* 37 (2019) 1851–1859.
[99] A.J. Susa, A.M. Ferris, D.F. Davidson, R.K Hanson, *AIAA J.* 57 (2019) 4476–4481.
[100] O.R. Yehia, C.B. Reuter, Y Ju, *Combust. Flame* 195 (2018) 63–74.
[101] O.R. Yehia, C.B. Reuter, Y Ju, *Proc. Combust. Inst.* 37 (2019) 1717–1724.
[102] M. Zhou, O.R. Yehia, C.B. Reuter, C.M. Burger, Y. Murakami, Y Ju, in: Proceedings of the 38 International Symposium on Combustion, 2020.
[103] A.G. Novoselov, C.B. Reuter, O.R. Yehia, et al., *Combust. Flame* 209 (2019) 144–154.
[104] Y. Murakami, C.B. Reuter, O.R. Yehia, Y Ju, Studies of autoignition-assisted nonpremixed cool flames, *Submitted to 38th International Symposium on Combustion*, 2020.
[105] W. Zhang, M. Faqih, X. Gou, Z Chen, *Combust. Flame* 187 (2018) 129–136.
[106] T. Zhang, A.J. Susa, R.K. Hanson, Y Ju, Autoignition assisted cool flame; double flame; spherical flame; flame speed; shock tube, *Submitted to 38th International Symposium on Combustion*, 2020.
[107] Y. Wang, H. Zhang, T. Zirwes, F. Zhang, H. Bockhorn, Z Chen, Ignition of dimethyl ether/air mixtures by hot particles: impact of low temperature chemical reactions, *Submitted to 38th International Symposium on Combustion*, 2020.
[108] Q. Yang, P. Zhao, Minimum ignition energy and propagation dynamics of laminar premixed cool flames, *Submitted to 38th International Symposium on Combustion*, 2020.

[109] A. Krisman, E.R. Hawkes, J.H Chen, *Combust. Flame* 188 (2018) 399–411.
[110] W. Liang, C.K. Law, *Combust. Flame* 185 (2017) 75–81.
[111] P. Zhao, C.K. Law, *Combust. Flame.* 160 (2013) 2352–2358.
[112] C.H. Sohn, H.S. Han, C.B. Reuter, Y. Ju, S.H Won, *Proc. Combust. Inst.* 36 (2017) 1329–1337.
[113] E. Lin, C.B. Reuter, Y Ju, *Proc. Combust. Inst.* 37 (2019) 1791–1798.
[114] R.N. Dahms, G.A. Paczko, S.A. Skeen, L.M Pickett, *Proc. Combust. Inst.* 36 (2017) 2615–2623.
[115] K. Seshadri, N. Peters, F.A. Williams, V. Nayagam, G Paczko, *Combust. Theory Model.* 20 (2016) 1118–1130.
[116] T. Farouk, Y. Xu, C. Avedisian, F Dryer, *Proc. Combust. Inst.* 36 (2017) 2585–2594.
[117] C. Law, *Prog. Energy Combust. Sci.* 8 (1982) 171–201.
[118] F.A. Williams, V Nayagam, *Combust. Flame* 212 (2020) 242–244.
[119] F.A. Williams, V. Nayagam, *Combust. Theory Model.* 23 (2019) 748–770.
[120] A.G. Novoselov, C.K. Law, M.E Mueller, *Proc. Combust. Inst.* 37 (2019) 2143–2150.
[121] A. Krisman, E.R. Hawkes, M. Talei, A. Bhagatwala, J.H Chen, *Proc. Combust. Inst.* 35 (2015) 999–1006.
[122] Y. Minamoto, J.H. Chen, *Combust. Flame* 169 (2016) 38–50.
[123] G. Borghesi, A. Krisman, T. Lu, J.H Chen, *Combust. Flame* 195 (2018) 183–202.
[124] T. Jin, Y. Wu, X. Wang, et al., *Appl. Energy* 249 (2019) 343–354.
[125] T. Zhou, M. Zhao, M. Zhu, T. Ye, M Liu, *Energy Fuels* 32 (2018) 9838–9849.
[126] H.K. Ciezki, G. Adomeit, *Combust. Flame* 93 (1993) 421–433.
[127] J. Shao, Y. Zhu, S. Wang, D.F. Davidson, R.K Hanson, *Fuel* 226 (2018) 338–344.
[128] S. Dooley, H.J. Curran, J.M Simmie, *Combust. Flame* 153 (2008) 2–32.
[129] S. Dooley, S.H. Won, M. Chaos, et al., *Combust. Flame* 157 (2010) 2333–2339.
[130] R. Minetti, M. Carlier, M. Ribaucour, E. Therssen, L Sochet, *Combust. Flame* 102 (1995) 298–309.
[131] S. Gallagher, H. Curran, W. Metcalfe, D. Healy, J. Simmie, G Bourque, *Combust. Flame* 153 (2008) 316–333.
[132] G. Mittal, S.M. Burke, V.A. Davies, B. Parajuli, W.K. Metcalfe, H.J Curran, *Combust. Flame* 161 (2014) 1164–1171.
[133] S.S. Goldsborough, S. Hochgreb, G. Vanhove, M.S. Wooldridge, H.J. Curran, C.-.J Sung, *Prog. Energy Combust. Sci.* 63 (2017) 1–78.
[134] C.K. Westbrook, J. Warnatz, W.J Pitz, in: Proceedings of the Symposium (international) on combustion, Elsevier, 1989, pp. 893–901.
[135] H. Curran, S. Fischer, F Dryer, *Int. J. Chem. Kinet.* 32 (2000) 741–759.
[136] P. Dagaut, M. Cathonnet, *Prog. Energy Combust. Sci.* 32 (2006) 48–92.
[137] C.K. Westbrook, W.J. Pitz, O. Herbinet, H.J. Curran, E.J Silke, *Combust. Flame* 156 (2009) 181–199.
[138] O. Herbinet, W.J. Pitz, C.K Westbrook, *Combust. Flame* 157 (2010) 893–908.
[139] W.K. Metcalfe, S.M. Burke, S.S. Ahmed, H.J Curran, *Int. J. Chem. Kinet.* 45 (2013) 638–675.
[140] O. Herbinet, F. Battin-Leclerc, *Int. J. Chem. Kinet.* 46 (2014) 619–639.
[141] Z. Wang, O. Herbinet, N. Hansen, F Battin-Leclerc, *Prog. Energy Combust. Sci.* 73 (2019) 132–181.
[142] J. Zádor, C.A. Taatjes, R.X Fernandes, *Prog. Energy Combust. Sci.* 37 (2011) 371–421.
[143] H.A. El-Asrag, Y.Ju, *Combust. Theory Modelling* 17 (2013) 316–334.
[144] H.A. El-Asrag, Y. Ju, in: Proceedings of the Fall Technical Meeting of the Eastern States Section of the Combustion Institute, Storrs, CT, University of Connecticut, October 9-12, 2011.
[145] Z. Zhao, M. Chaos, A. Kazakov, F.L Dryer, *Int. J. Chem. Kinet.* 40 (2008) 1–18.
[146] M. Barusch, H. Crandall, J. Payne, J Thomas, *Ind. Eng. Chem.* 43 (1951) 2764–2766.
[147] J. Knox, *Combust. Flame* 9 (1965) 297–310.
[148] C. Morley, in: Proceedings of the Symposium (International) on Combustion, Elsevier, 1989, pp. 911–918.
[149] M. Carlier, C. Corre, R. Minetti, J. Pauwels, M. Ribaucour, L Sochet, in: Proceedings of the Twenty-Third Symposium (International) on Combustion, 1758, The Combustion Institute, 1753, p. 1990.
[150] A. Fish, *Chem. Soc.* 18 (1964) 243–269.
[151] S.W. Benson, *J. Am. Chem. Soc.* 87 (1965) 972–979.
[152] H.J. Curran, *Proc. Combust. Inst.* 37 (2019) 57–81.
[153] M.R. Harper, K.M. Van Geem, S.P. Pyl, G.B. Marin, W.H Green, *Combust. Flame* 158 (2011) 16–41.
[154] Z. Wang, S.M. Sarathy, *Combust. Flame* 165 (2016) 364–372.
[155] Z. Wang, D.M. Popolan-Vaida, B. Chen, et al., *Proc. Natl. Acad. Sci.* 114 (2017) 13102–13107.
[156] R.T. Skodje, A.S. Tomlin, S.J. Klippenstein, L.B. Harding, M.J Davis, *J. Phys. Chem. A* 114 (2010) 8286–8301.
[157] H. Hashemi, J.M. Christensen, L.B. Harding, S.J. Klippenstein, P Glarborg, *Proc. Combust. Inst.* 37 (2019) 461–468.
[158] J. Powling, *Fuel* 28 (1949) 25–28.
[159] R. Fairlie, J. Griffiths, H Pearlman, *Proc. Combust. Inst.* 28 (2000) 1693–1699.
[160] R. Fairlie, J. Griffiths, K. Hughes, H Pearlman, *Proc. Combust. Inst.* 30 (2005) 1057–1064.
[161] H.J. Curran, P. Gaffuri, W.J. Pitz, C.K Westbrook, *Combust. Flame* 129 (2002) 253–280.
[162] M. Hori, H. Nakamura, T. Tezuka, S. Hasegawa, K Maruta, *Proc. Combust. Inst.* 34 (2013) 3419–3426.
[163] T. Kamada, H. Nakamura, T. Tezuka, S. Hasegawa, K Maruta, *Combust. Flame* 161 (2014) 37–48.
[164] T. Shimizu, H. Nakamura, T. Tezuka, S. Hasegawa, K Maruta, *Energy Fuels* 31 (2017) 2298–2307.
[165] P. Grajetzki, H. Nakamura, T. Tezuka, S. Hasegawa, K Maruta, *Fuel* 245 (2019) 429–437.
[166] S. Wan, Y. Fan, K. Maruta, Y Suzuki, *Proc. Combust. Inst.* 37 (2019) 5655–5662.
[167] Y.Ju, C.B. Reuter, S.H Won, *Combust. Flame* 162 (2015) 3580–3588.
[168] Y. Ju, *Combust. Flame* 178 (2017) 61–69.

[169] Y.Ju, H. Guo, K. Maruta, F Liu, *J. Fluid Mech.* 342 (1997) 315–334.
[170] P.Zhao, W.Liang, S. Deng, C.K Law, *Fuel* 166 (2016) 477–487.
[171] S.H. Won, W.Sun, Y Ju, *Combust. Flame* 157 (2010) 411–420.
[172] S.H. Won, S. Dooley, F.L. Dryer, Y Ju, *Proc. Combust. Inst.* 33 (2011) 1163–1170.
[173] S.H. Won, S. Dooley, F.L. Dryer, Y Ju, *Combust. Flame* 159 (2012) 541–551.
[174] J.K. Lefkowitz, S.H. Won, Y.Fenard, Y Ju, *Proc. Combust. Inst.* 34 (2013) 813–820.
[175] J.E. Harrington, K.C. Smyth, *Chem. Phys. Lett.* 202 (1993) 196–202.
[176] U. Niemann, K. Seshadri, F.A Williams, *Combust. Flame* 162 (2015) 1540–1549.
[177] Z. Wang, X. Zhang, L. Xing, et al., *Combust. Flame* 162 (2015) 1113–1125.
[178] T. Ombrello, C. Carter, V Katta, *Combust. Flame* 159 (2012) 2363–2373.
[179] T.I. Farouk, Y.Xu, C.T. Avedisian, F.L Dryer, *Proc. Combust. Inst.* 36 (2017) 2585–2594.
[180] M. Chaos, A. Kazakov, Z. Zhao, F.L Dryer, *Int. J. Chem. Kinet.* 39 (2007) 399–414.
[181] https://spaceflightsystems.grc.nasa.gov/sopo/ihho/psrp/fcf/fcf-investigations/acme/.
[182] T. Farouk, F Dryer, *Combust. Theory Model.* 15 (2011) 487–515.
[183] T. Farouk, F.L. Dryer, *Combust. Flame* 159 (2012) 200–209.
[184] S. Liu, J.C. Hewson, J.H. Chen, H Pitsch, *Combust. Flame* 137 (2004) 320–339.
[185] N. Kurimoto, B. Brumfield, X. Yang, et al., *Proc. Combust. Inst.* 35 (2015) 457–464.
[186] O.R. Yehia, C.B. Reuter, Y Ju, *Combust. Flame* 195 (2018) 63–74 in press.
[187] L. Cai, A. Sudholt, D.J. Lee, et al., *Combust.Flame* 161 (2014) 798–809.
[188] Y.Ju, J.K. Lefkowitz, C.B. Reuter, et al., *Plasma Chem. Plasma Process.* 36 (2016) 85–105.
[189] H. Zhao, L. Wu, C. Patrick, et al., *Combust. Flame* 197 (2018) 78–87.
[190] H. Zhao, A.G. Dana, Z. Zhang, W.H. Green, Y Ju, *Energy* 165 (2018) 727–738.
[191] L. Marrodán, Y. Song, O. Herbinet, et al., *Chem. Phys. Lett.* 719 (2019) 22–26.
[192] L. Marrodán, Y. Song, M. Lubrano Lavadera, et al., *Energy Fuels* 33 (2019) 5655–5663.
[193] P. Dagaut, J. Luche, M Cathonnet, *Combust. Sci. Technol.* 165 (2001) 61–84.
[194] T. Am Ano, F.L Dryer, in: Proceedings of the Symposium (International) on Combustion, 1998, pp. 397–404.
[195] S. Thion, C. Togbé, Z. Serinyel, G. Dayma, P Dagaut, *Combust. Flame* 185 (2017) 4–15.
[196] L.S. Tran, O. Herbinet, Y. Li, et al., *Proc. Combust. Inst.* 37 (2019) 511–519.
[197] A. Krisman, E.R. Hawkes, M. Talei, A. Bhagatwala, J.H Chen, *Proc. Combust. Inst.* 36 (2017) 3567–3575.
[198] A. Krisman, E.R. Hawkes, J.H Chen, *Proc. Combust. Inst.* 37 (2019) 4787–4795.
[199] T. Jin, K.H. Luo, X. Wang, K. Luo, J Fan, *Proc. Combust. Inst.* 37 (2019) 4625–4633.
[200] Z. Chen, M. Burke, Y Ju, *Proc. Combust. Inst.* 32 (2009) 1253–1260.
[201] Z. Chen, M.P. Burke, Y Ju, *Proc. Combust. Inst.* 33 (2011) 1219–1226.
[202] Z. Chen, Y. Ju, *Combust. Theory Modelling* 11 (2007) 427–453.
[203] A.W. Skiba, T.M. Wabel, C.D. Carter, S.D. Hammack, J.E. Temme, J.F Driscoll, *Combust. Flame* 189 (2017) 407–432.
[204] A. Krisman, E.R. Hawkes, J.H Chen, *J. Fluid Mech.* 824 (2017) 5–41.
[205] B. Savard, H. Wang, A. Teodorczyk, E.R Hawkes, *Combust. Flame* 196 (2018) 71–84.
[206] S.H. Won, B. Windom, B. Jiang, Y Ju, *Combust. Flame* 161 (2014) 475–483.
[207] B. Windom, S.H. Won, C.B. Reuter, et al., *Combust. Flame* 169 (2016) 19–29.
[208] G. Bansal, A. Mascarenhas, J.H Chen, *Combust. Flame* 162 (2015) 688–702.
[209] A. Krisman, E.R. Hawkes, M. Talei, A. Bhagatwala, J.H Chen, *Combust. Flame* 172 (2016) 326–341.
[210] S. Skeen, J. Manin, L.M Pickett, *SAE Int. J. Engines* 8 (2015) 696–715.
[211] L.M. Pickett, S. Kook, T.C Williams, *SAE Int. J. Engines* 2 (2009) 439–459.
[212] U. Burke, K.P. Somers, P. O'Toole, et al., *Combust. Flame* 162 (2015) 315–330.
[213] E.E. Dames, A.S. Rosen, B.W. Weber, C.W. Gao, C.-J. Sung, W.H Green, *Combust. Flame* 168 (2016) 310–330.
[214] H. Zhao, X. Yang, Y Ju, *Combust. Flame* 173 (2016) 187–194.
[215] C.B. Reuter, R. Zhang, O.R. Yehia, Y.Rezgui, Y Ju, *Combust. Flame* 196 (2018) 1–10.
[216] O. Herbinet, W.J. Pitz, C.K Westbrook, *Combust. Flame* 154 (2008) 507–528.
[217] M. Mehl, W.J. Pitz, C.K. Westbrook, H.J Curran, *Proc. Combust. Inst.* 33 (2011) 193–200.
[218] S. Dooley, S.H. Won, J. Heyne, et al., *Combust. Flame* 159 (2012) 1444–1466.
[219] J. Yu, Y. Ju, X Gou, *Fuel* 166 (2016) 211–218.
[220] S.M. Sarathy, C.K. Westbrook, M. Mehl, et al., *Combust. Flame* 158 (2011) 2338–2357.
[221] W.Sun, Z. Chen, X. Gou, Y Ju, *Combust. Flame* 157 (2010) 1298–1307.
[222] D.F. Davidson, S.C. Ranganath, K.Y. Lam, M. Liaw, Z. Hong, R.K Hanson, *J. Propul. Power* 26 (2010) 280–287.
[223] S.G. Davis, C.K. Law, *Combust. Sci. Technol.* 140 (1998) 427–449.
[224] R. Grana, K. Seshadri, A. Cuoci, U. Niemann, T. Faravelli, E Ranzi, *Combust. Flame* 159 (2012) 130–141.
[225] C. Ji, E. Dames, Y.L. Wang, H. Wang, F.N Egolfopoulos, *Combust. Flame* 157 (2010) 277–287.
[226] A.P. Kelley, A.J. Smallbone, D.L. Zhu, C.K Law, *Proc. Combust. Inst.* 33 (2011) 963–970.
[227] H.-.P.S. Shen, J. Steinberg, J. Vanderover, M.A Oehlschlaeger, *Energy Fuels* 23 (2009) 2482–2489.
[228] A.T. Holley, Y. Dong, M.G. Andac, F.N. Egolfopoulos, T Edwards, *Proc. Combust. Inst.* 31 (2007) 1205–1213.
[229] J.T.D. Piazza, M. Gerstein, R.C Weast, *Ind. Eng. Chem.* 43 (1951) 2721–2725.
[230] F.L. Dryer, *Proc. Combust. Inst.* 35 (2015) 117–144.

[231] K. Zhang, C. Banyon, J. Bugler, et al., *Combust. Flame* 172 (2016) 116–135.
[232] C.B. Reuter, R. Zhang, O.R. Yehia, Y. Rezgui, Y. Ju. Counterflow Flame Experiments and Chemical Kinetic Modeling of Dimethyl Ether/Methane Mixtures. Submitted to Combustion and Flame. 2018.
[233] J.C. Prince, F.A. Williams, *Combust. Flame* 162 (2015) 3589–3595.
[234] Z. Li, W. Wang, Z. Huang, M.A Oehlschlaeger, *Energy Fuels* 27 (2013) 2811–2817.
[235] !!! INVALID CITATION !!! [227-230].
[236] F. Battin-Leclerc, O. Herbinet, P.A. Glaude, et al., *Angew. Chem. Int. Ed.* 49 (2010) 3169–3172.
[237] C.A. Taatjes, G. Meloni, T.M. Selby, et al., *J. Am. Chem. Soc.* 130 (2008) 11883–11885.
[238] K. Moshammer, A.W. Jasper, D.M. Popolan–Vaida, et al., *J. Phys. Chem. A* 119 (2015) 7361–7374.
[239] M. Blocquet, C. Schoemaecker, D. Amedro, O. Herbinet, F. Battin-Leclerc, C Fittschen, *Proc. Natl. Acad. Sci.* 110 (2013) 20014–20017.
[240] B. Brumfield, W. Sun, Y. Ju, G Wysocki, *J. Phys. Chem. Lett.* 4 (2013) 872–876.
[241] C.-.H. Wang, Masunov AmE, T.C. Allison, et al., *J. Phys. Chem. A* (2019).
[242] O.V. Skrebkov, *Combust. Theory Model.* 19 (2015) 131–158.
[243] M.P. Burke, S.J. Klippenstein, *Nat. Chem.* 9 (2017) 1078–1082.
[244] H. Zhao, C. Yan, T. Zhang, et al., in: Proceedings of the 38 International Symposium on Combustion, 2020.
[245] C.F. Goldsmith, L.B. Harding, Y. Georgievskii, J.A. Miller, S.J Klippenstein, *J. Phys. Chem. A* 119 (2015) 7766–7779.
[246] H. Zhong, C. Yan, C.C. Teng, G. Ma, G. Wysocki, Y Ju, in: Proceedings of the 38 International Symposium on Combustion, 2020.
[247] S.J. Klippenstein, *Proc. Combust. Inst.* 36 (2017) 77–111.
[248] H. Wang, D.A. Sheen, *Prog. Energy Combust. Sci.* 47 (2015) 1–31.
[249] R. Ramakrishnan, P.O. Dral, M. Rupp, O.A von Lilienfeld, *J. Chem. Theory Comput.* 11 (2015) 2087–2096.
[250] A.R. Singh, B.A. Rohr, J.A. Gauthier, J.K Nørskov, *Catal. Lett.* 149 (2019) 2347–2354.
[251] H. Zhong, M.N. Shneider, M.S. Mokrov, Y Ju, *J. Phys. D Appl. Phys.* 52 (2019) 484001.
[252] Z. Wang, H. Liu, T. Song, et al., *Int. J. Engine Res.* 16 (2015) 166–180.
[253] Sun W., Wang L., Grenga T., Ju Y. Development of a Multiscale Adaptive Reduced Chemistry Solver (MARCS) for Computationally Efficient Combustion Simulations.
[254] T. Zhang, W. Sun, Y Ju, *Proc. Combust. Inst.* 36 (2017) 1539–1547.
[255] Tianhan Zhang, Weiqi Sun, Liang Wang, Ju Y. Effects of Low Temperature Chemistry and Turbulence Transport on Knocking Formation for Stratified Dimethyl Ether/Air Mixtures Combustion and Flame, submitted. 2018.
[256] P. Dai, Z. Chen, S. Chen, Y Ju, *Proc. Combust. Inst.* 35 (2015) 3045–3052.
[257] Juan Sepulveda, Aric Rousso, Henry Ha, et al., *AIAA J.* 57 (2019) 476–481.
[258] J. Crane, X. Shi, A.V. Singh, Y. Tao, H Wang, *Combust. Flame* 200 (2019) 44–52.